SANDIA REPORT

SAND98–2101
Unlimited Release
Printed September 1998

Rapid Melt and Resolidification of Surface Layers Using Intense, Pulsed Ion Beams Final Report

Tim Renk, Bob Turman, Donna Senft, Neil R. Sorensen, Regan Stinnett, John B. Greenly, Michael O. Thompson, Rudolph G. Buchheit

Prepared by
Sandia National Laboratories
Albuquerque, New Mexico 87185 and Livermore, California 94550

Sandia is a multiprogram laboratory operated by Sandia Corporation, a Lockheed Martin Company, for the United States Department of Energy under Contract DE-AC04-94AL85000.

Sandia National Laboratories

Issued by Sandia National Laboratories, operated for the United States Department of Energy by Sandia Corporation.

Available to DOE and DOE contractors from
Office of Scientific and Technical Information
P.O. Box 62
Oak Ridge, TN 37831

Prices available from (615) 576-8401, FTS 626-8401

Available to the public from
National Technical Information Service
U.S. Department of Commerce
5285 Port Royal Rd
Springfield, VA 22161

NTIS price codes
Printed copy: A04
Microfiche copy: A01

SAND98-2101
Unlimited Release
Printed September, 1998

Rapid Melt And Resolidification Of Surface Layers Using Intense, Pulsed Ion Beams
Final Report

Tim Renk
Bob Turman
Beam Applications and Initiatives Department

Donna Senft
Neil R. Sorensen
Materials Aging & Reliability: Interfaces Department

Sandia National Laboratories
P. O. Box 5800
Albuquerque, NM 87185-1182

Regan Stinnett
Quantum Manufacturing Technologies, Inc.
3701 Hawkins Street, NE
Albuquerque, NM 87109

John B. Greenly
Michael O. Thompson
Cornell University, Ithaca, New York

Rudolph G. Buchheit
Ohio State University, Columbus, Ohio

Abstract

The emerging technology of pulsed intense ion beams has been shown to lead to improvements in surface characteristics such as hardness and wear resistance, as well as mechanical smoothing. We report here on the use of this technology to systematically study improvements to three types of metal alloys – aluminum, iron, and titanium. Ion beam treatment produces a rapid melt and resolidification (RMR) of the surface layer. In the case of a predeposited thin-film layer, the beam mixes this layer into the substrate, leading to improvements that can exceed those produced by treatment of the alloy alone. In either case, RMR results in both crystal refinement and metastable state formation in the treated surface layer not accessible by conventional alloy production. Although more characterization is needed, we have begun the process of relating these microstructural changes to the surface improvements we discuss in this report.

Table of Contents

1.0 Introduction

For the past 40 years researchers have investigated the production of rapidly solidified metallurgical microstructures using techniques ranging from melt quenching and spray deposition to liquid metal casting[1,2,3].These techniques use the principle of rapid cooling by heat transfer from the liquid metal to an adjoining cool surface to achieve cooling rates of 10^6 K/sec. The metastable phases produced by rapid solidification[4] have enhanced properties including improved corrosion and wear resistance and increased hardness.

The demonstrated capabilities of rapid solidification of liquid metals are impressive, including the following examples:

1. Improved hardness and wear resistance in tool steels[5] and aluminum die castings[6],
2. Improved corrosion resistance in both amorphous[7] and microcrystalline states[8] as well as in conventional stainless steels[9,10,11],
3. Enhanced fatigue behavior in Ti-6Al-4V alloy (widely used in aerospace and biomedical applications),
4. Metastable surface alloys providing order-of-magnitude increases in wear resistance in tool steels[12], and
5. Improved fatigue, wear, and heat resistance in metastable Al-Si-Fe alloys[13,14].

Continuous and pulsed laser beams have been used to provide the high power densities needed to melt metal surface layers, resulting in rapid cooling of the melted layer by thermal diffusion into the underlying, unheated material. Experiments using the extremely rapid cooling rates (10^7-10^{11} K/sec) resulting from laser treatment have demonstrated the usefulness of producing near-surface layers with non-equilibrium microstructures including amorphous and fine grain layers and metastable phase alloys with extended solubility limits. The faster quench rates (compared to the 10^6 K/s typical for earlier techniques such as splat quenching) extend the benefits of Rapid Melt and Resolidification (RMR) to more alloys and improve the results. The ability to enhance surface properties by producing non-equilibrium surface layers is important because the performance of materials in specific applications is strongly affected by their surface properties.

The demonstrated beneficial effects of short-pulse thermal surface treatment by directed energy beams include improved corrosion, friction, wear, and hardness properties of metal surfaces. These have been demonstrated using short pulsed lasers[15,16,17,18,19] and in single pulse ion beam experiments in Russia[20,21,22], Japan[23] and the US[24,25,26]. Some of these effects have begun to be used in high value applications in industry such as CO_2 laser treatment of cam shafts and valve seats.

In spite of the encouraging results obtained in rapid resolidification experiments using lasers, widespread commercial use of this technology has been prevented by several problems intrinsic to laser technology. These limiting factors include inefficient energy coupling to metal surfaces, surface roughening by local vaporization, low electrical efficiency, small treatment spot size, and the high cost of laser systems with commercially useful average powers.

Early pulsed ion beam experiments have also suffered from major problems, including the inability to produce repetitive pulses and problems with purity, lifetime, and debris from passive ion sources. These problems can now be solved by the use of a new repetitively pulsed, long component lifetime, intense ion beam technology for thermal surface treatment developed at Sandia National Laboratories, Cornell University[27,28,29], and, more recently, at QMT Technologies (Albuquerque). Researchers have developed the capability to produce 5-250

kW average power pulsed ion beams at 0.2-2 MeV energies. This new capability is enabling us to develop a commercial-scale thermal surface treatment technology called Ion Beam Surface Treatment (IBEST). This technique uses high energy, pulsed (typically $\leq$100 ns) ion beams to deposit energy directly in the top 2-20 micrometers of the surface of any material. Because only $3x10^{13}$ ions/cm^2 per pulse are needed to melt the surface, the implanted ion concentration is less than 10^{-3} atomic percent over the ion range, making implantation or hydrogen embrittlement effects negligible.

Using IBEST, the depth of treatment is controllable by varying the ion energy and species. Deposition of the energy in a thin surface layer (Figure 1) allows melting of the layer with relatively small energies (1-10 J/cm^2 for metal surfaces) and allows rapid cooling of the melted layer by thermal diffusion into the underlying substrate. Typical cooling rates of this process (10^9-10^{10} K/sec) are sufficient to cause amorphous layer formation and the production of non-equilibrium microstructures (nano-crystalline and metastable phases). Exploratory experiments with ion beams[20,21,22,26] have shown that surfaces produced by this rapid thermal quenching may have significantly improved corrosion, wear, and hardness properties.

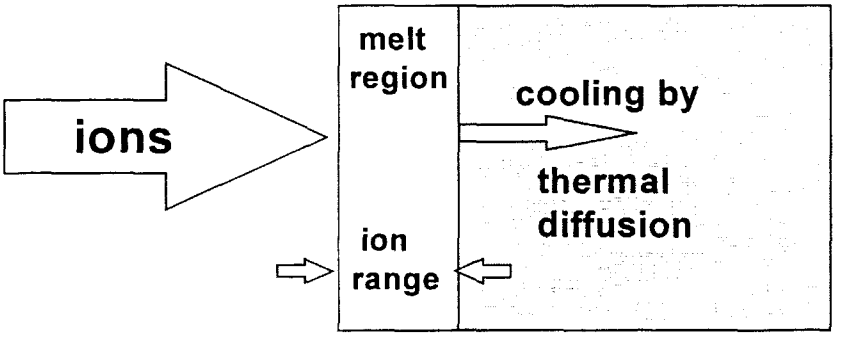

Figure 1. Ion Beam Surface Treatment (IBEST) uses a pulsed, high energy (0.2-2 MeV) ion beam to deposit energy over the classical ion range, typically 2-20 microns, in a surface, raising its temperature to melt. Thermal diffusion rapidly (10^9 - 10^{10} K/sec) cools the surface, leading to the formation of amorphous layers and the production of non-equilibrium microstructures by rapid quenching.

The short pulse length used in this technology allows the heated depth to be confined to approximately the ion range by limiting the effect of thermal diffusion. Thermal diffusion lengths in 60 ns are 1 and 4 microns in stainless steel and aluminum respectively, less than the proton range in the materials at typical IBEST ion energies of 0.4-1 MeV. Energy deposition by high energy ions is well understood in the parameter range used by IBEST. Ions lose energy to the electrons and atoms of a material by Coulombic interactions. For IBEST parameters (e.g. proton energy >> 10 keV) energy transfer is predominantly (>98%) due to the electrons, resulting in rapid (<<1 ns) conversion to heat. Protons, having the largest ion range in materials, can provide relatively deep treatment as illustrated in Figure 2.

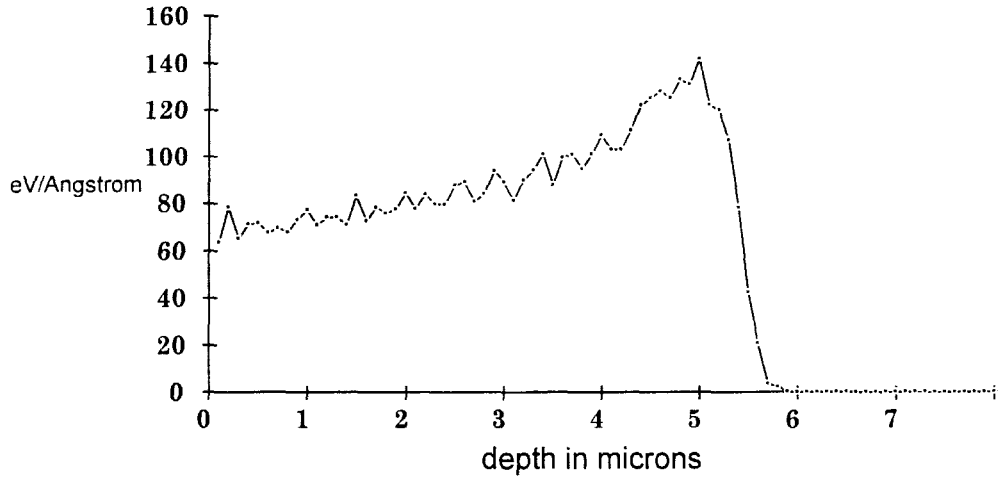

Figure 2. This TRIM code-calculated energy deposition profile for normally incident 500 keV protons into aluminum illustrates the intrinsic in-depth treatment capability of IBEST technology.

Under this project sponsored by the Division of Advanced Energy Technology, we studied the effects of rapid melt and resolidification of metal surfaces (RMR) using intense, pulsed, high voltage (0.4-1 MeV) ion beams. This effort was directed toward achieving basic understanding of the capabilities and limitations of RMR of materials in the parameter ranges of quench rate and melt depth made possible by our new IBEST technology.

The following tasks were accomplished during this project, and results are presented in this report.

Task 1. Surface Microstructure Modification and Modeling

Identify the microstructures formed under the range of quench conditions (10^{9}-10^{10} K/s) produced by IBEST in common ferrous and non-ferrous alloys using X-Ray diffraction (XRD) and cross-sectional transmission electron microscopy (XTEM). Calculate the time and depth-resolved ion energy deposition and temperature history of ferrous and non-ferrous materials and correlate with experiments. Measure the time-to-melt, and time-resolved temperature profiles. Use these to benchmark a 1-dimensional model.

Task 2. Corrosion and Wear Resistance Treatment

Demonstrate that IBEST/RMR imparts desirable levels of corrosion resistance in non-heat-treatable aluminum alloys (e.g., 3003), heat treatable aluminum alloys (e.g., 2024, 6061, 7075), cast aluminum (e.g., A356), precipitation hardened stainless steel (e.g., 17-4PH) and sensitized and unsensitized austenitic stainless steels (e.g., 304, 316, 321). Verify enhanced performance using electrochemical and accelerated exposure testing and identify relevant microstructure property relationships. Demonstrate that IBEST/RMR can induce liquid phase mixing of a pre-deposited metal layer with the alloy surface to produce corrosion-resistant layers such as Al-Cr, Al-Hf, Al-W, Al-Ta, Fe-Cr, and Ti-Pd. Verify enhanced tribological properties of RMR martensitic stainless steel (e.g. 440C). Identify minimum criteria (e.g., depth of treatment, time above melt, minimum absolute temperature achieved, total energy deposited) for selecting the beam regime required to achieve desired performance.

Task 3. Surface Alloy Formation

Study liquid phase diffusion across rapidly melted and quenched interfaces between thin film coatings of metal on metal or silicon substrates. Analyze the microstructure of samples exposed to single and multiple heating/quenching cycles. Identify possible new, non-equilibrium alloys formed from elements that are normally immiscible. Characterize the interfacial reaction using techniques such as Rutherford

Backscattering Spectroscopy (RBS), Secondary Ion Mass Spectrometry (SIMS), AES with sputter profiling, and XTEM

Task 4. Surface Smoothing and Densification

Study the capability of IBEST to smooth, densify, and heal defects in surfaces by rapid melt and resolidification of metal, ceramic and plasma sprayed surfaces. Study the effects of varying incident ion energy and number of pulses. Measure topological and microstructural changes using scanning electron microscopy.

2.0 Experimental IBEST Treatment Facility

Until recently, pulsed ion beams have not been considered a viable technology for routine materials processing applications because of their inability to deliver the multi-kilowatt average powers with long component lifetimes needed for commercial processing applications. During the past few years there has been significant progress in two complementary technologies that now enable the design of high power, long lifetime ion beam surface treatment systems for materials processing. These are repetitive pulsed power (RHEPP) and ion beam (MAP) technologies.

The first of these advances is the development of a compact, electrically efficient, repetitively pulsed, magnetically switched pulsed power system capable of 10^9 pulse component lifetimes. This prototype system, the Repetitive High Energy Pulsed Power-I (RHEPP-I) facility[27] (0.8 MV, 35Ω, 60 ns FWHM pulse duration, 120 Hz repetition frequency) began operation in 1993 at Sandia National Laboratories. This system, shown in Figure 3, has demonstrated operation at 50% electrical efficiency from the wall plug to a matched load. Its capability to efficiently produce high average power, high voltage electrical pulses using a compact design is a breakthrough for the commercial application of pulsed power.

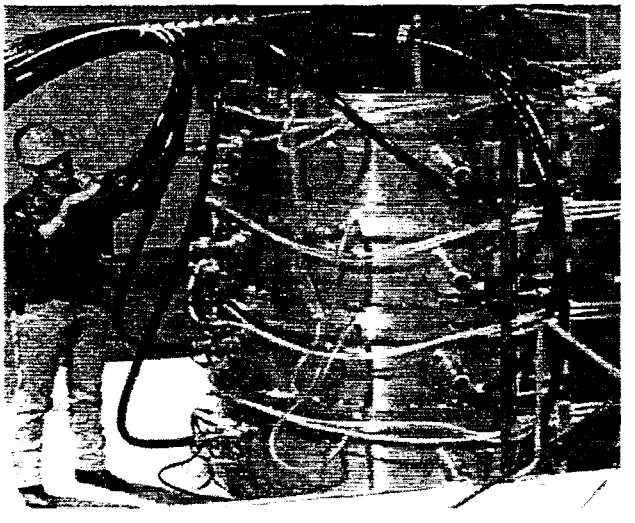

Figure 3. The Repetitive High Energy Pulsed Power facility at Sandia National Laboratories became operational in April 1993. It is designed to deliver 0.8 MeV, 60 ns, 25 kA pulses at the rate of 120 Hertz with 50% electrical efficiency.

The second advance is an ion beam system that is capable of operating repetitively and efficiently to transform the pulsed power of RHEPP into an ion beam. An ion beam system capable of operating at repetitive pulse rates of 100 Hz in 10 pulse burst mode (active cooling was not part of the design) was demonstrated [28,29] at the Cornell University Laboratory of Plasma Studies, producing ion beams at 20 kA

and 100 kV. An improved version of this system is now being fielded on the RHEPP-I facility at Sandia. This system, the Magnetically-confined Anode Plasma (MAP) ion source, shown in Figure 4, is based on the concept of drawing ions from a single species plasma anode rather than the solid, flashover anode used in standard single pulse ion beam systems. The plasma can be created using any gas ion to produce a preformed, selectable species, ionized gas anode to provide a pure, uniform ion beam without debris.

Figure 4. The Magnetically confined Anode Plasma (MAP) ion beam system for RHEPP is a scale up of previous, repetitively pulsed MAP systems used successfully at Cornell University.

The MAP ion beam system produces an annular beam which is brought to a broad focus symmetric about the axis shown in Figure 5. In the cathode (ground potential) electrode assembly (A), slow (100 μs rise time) magnetic field coils (B) produce magnetic flux which provides the magnetic insulation of the accelerating gap between the cathode and the anode (high voltage) electrode assembly (C) connected to the output of the RHEPP generator. The ion source that supplies ions to the accelerating gap is contained within the anode assembly. The MAP source operates in the following way: a fast gas valve (D) on the axis of the anode assembly produces a rapid gas puff which is delivered through a supersonic nozzle (E) to produce a highly localized volume of gas (F) directly in front of the surface of a fast-driving coil (G) located in an insulating support structure (H). After preionization by an induced electric field, the fast coil is energized, inducing a loop voltage of 20 kV on the gas volume, driving a breakdown to full ionization, and moving the resulting plasma toward the flux-excluding anode field-shaping electrodes (C) in about 1.5 μs to form a thin magnetically-confined plasma layer. The high voltage pulse is then applied to the anode assembly, accelerating ions from this plasma layer to form the ion beam. The magnetic flux surfaces (J) at the time of beam extraction are shown. The beam propagates in vacuum to a broad focal area at the target plane at the right of the figure, where material samples are placed for treatment.

Under a Cooperative Research and Development Agreement (CRADA) with QM Technologies, a compact version of RHEPP and MAP technology has been developed for processing applications. This will allow IBEST technology to be more widely available.

An alternative source used on some experiments is an epoxy-filled groove or "flashover" anode. The grooves are located in place of the annulus defined by the inner and outer flux excluders. When the power pulse arrives, the triple-point stress at the corners of the grooves breaks down, leading to the formation of a dense plasma from which the beam is extracted. The beam is initially composed of protons (about 30% of the total), then carbon for the remainder of the pulse. Some samples treated with the flashover source yielded significant performance gain, such as the 440C samples discussed in Section 4.2. Since this type of ion source is not robust, we have used the MAP source to treat almost all of the recently processed samples.

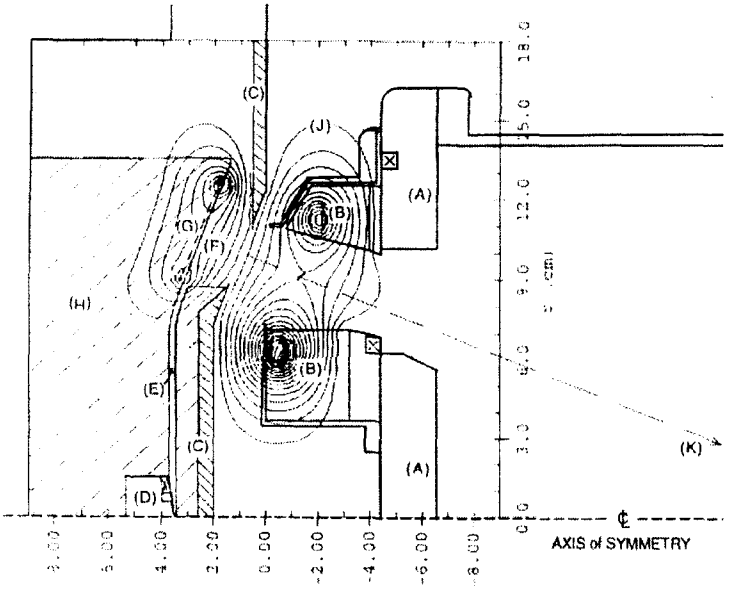

Figure 5. MAP Ion Diode for RHEPP. The cathode assembly (A) with slow magnetic field coils (B); the anode electrodes/magnetic flux shapers (C); the fast gas valve (D); the gas nozzle (E); the gas breakdown and plasma formation region (F); the fast-driving magnetic field coil (G) in the insulation support structure (H), the magnetic flux of the slow and fast coils, as they are at the time of the RHEPP accelerating pulse (J); the ion beam propagation direction to the material target (K).

3.0 Ion Beam Surface Interaction Modeling and Experiment

3.1 Beam-Matter Interaction Modeling

Ion energy deposition in materials is well described by classical, collisional processes. Time and depth-dependent temperature in a sample have been modeled using the TRIM code[30] together with a new, one-dimensional, finite element code[31] that incorporates basic materials properties. The information provided by this code allows us to understand local conditions in treated samples and correlate them with experimentally measured changes in microstructure. The code numerically solves the heat equation:

$$\rho C_p(\partial/\partial t)T(x,t) = (\partial/\partial x)[k(x,t)(\partial/\partial x)T(x,t)] + S(x,t)$$

where ρ is the mass density, C_p is the specific heat of the material, k is the thermal conductivity, T is the temperature, x is the depth into the target, t is the time. S(x,t) is the source/sink term including the time and space-dependent beam energy deposition from the pulse waveform and TRIM calculations and includes latent heat losses from phase changes. This model also accounts for the energy involved in solid to liquid phase changes but does not include hydrodynamics and radiation losses. This is because for the cases discussed in this report, we restrict beam fluences to levels where surface vaporization is not a significant factor. This l-D model is adequate, since the beam diameter is always much greater than the treated depth.

Detailed benchmarking of simulation with experiment are presented in the next section, where calculated and measured melt durations of the the surface of Si are presented. We have also compared melt depths predicted by the model with metal samples that have been treated and then cross-sectioned.

As an example, a Ti Grade 5 sample was subjected to a nitrogen beam (25 pulses). Two Faraday cups nearest the sample location indicated a fluence range between 2.5 and 2.8 J/cm^2. These values were input to the code, which predicted a melt depth of between 2.2 and 2.45 microns, very close to the measured 2.5 micron depth. In Figure 6 we show the calculated[31] local temperatures using an ion pulse waveform from the RHEPP-I facility (2.68 J/cm^2, 200 ns FWHM at sample location, peak voltage 630 kV) for treatment of titanium. Temperatures exceeding the melt point are calculated to occur over a depth of about 2.2 microns.

Cooling rates exceeding 10^9 K/sec are calculated. Note also that, in this case, surface temperatures exceeding the vaporization point of Ti are expected to occur over about 200 ns. Thus, we have induced some amount of vaporization at this fluence level.

Additionally, a sample of Al 6061 was treated with the flashover source and sectioned. Three locations were measured for melt depth and compared to the code predictions for the three fluences (3.5, 2.3, and 1.5 J/ cm^2, respectively). The measured depths ranged from 7 microns at the highest fluence, to 2 - 2.5 microns for the intermediate fluence, to almost zero for the lowest fluence. Code predictions were: 5.6 microns at the highest fluence, 2.8 microns, and 0.15 microns at the lowest fluence. The quantitative and scaling agreement between code and measurement are thus very close. Measurements and calculations with silicon material are presented in the next section.

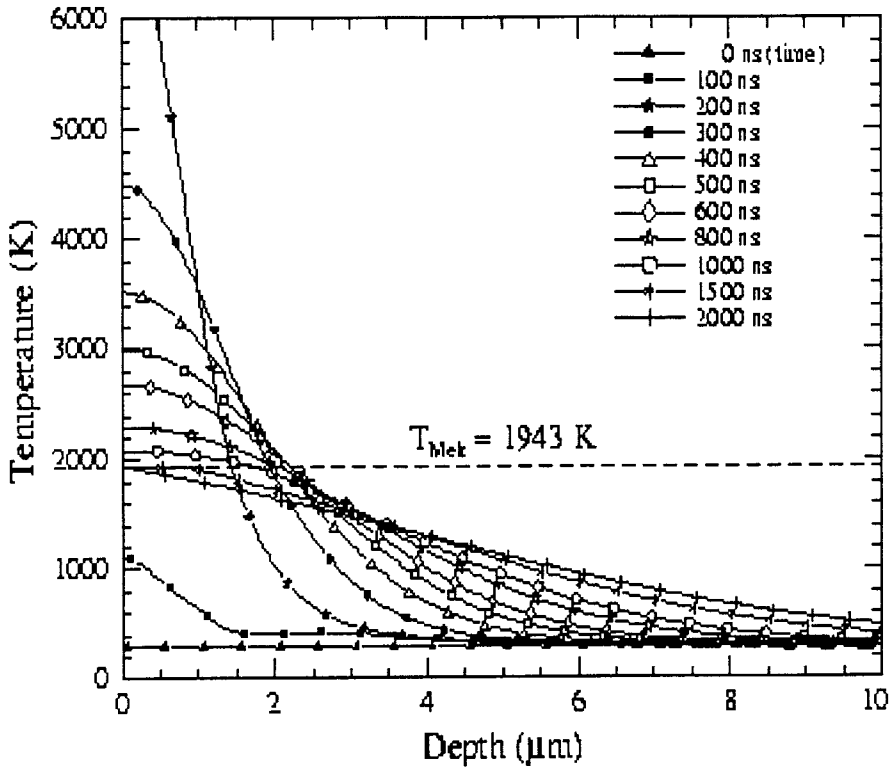

Figure 6. These are results from one dimensional modeling of ion deposition and heating of Ti-5 using a pulse of 2.68 J/cm^2 intensity, consisting of approximately 10% protons, 35% N+2, and 55% N+1. Peak voltage was 630 kV, and peak beam current was 50 A/ cm^2.

3.2 Laser Reflectometry Experiments

A laser reflectometer diagnostic was developed to directly observe the melt and resolidification of a surface that is exposed to the pulsed ion beam. This technique was tested with a high-purity silicon substrate, to benchmark the melt duration and melt depth calculations from the 1-D model. Silicon was chosen for this test because of the availability of an extensive thermal data set, and because the behavioral change of its reflection coefficient between solid and liquid phases is distinct. In contrast, the reflection coefficient of most metals is a more complex function of surface temperature, so that direct measurements are more ambiguous than with Si. The technique is based on observation of changes in surface reflectance as the surface melts and then resolidifies. A solid-state laser, fiber optic, and photodiode are arranged to make this reflectance measurement in real-time as the sample is being pulsed by the high intensity ion beam, as shown in Fig. 7. Sample traces of the reflected laser light are shown in the left side of the figure. With silicon, the reflectance of the surface increases upon melting, and again reduces upon resolidification. This property is observed in the waveforms, and the duration of the melt phase is clearly seen in the data. Experimentally, the melt duration is determined by the time during which the reflected signal level is more than 10% of its maximum value. Faraday cups observing near the sample gave absolute beam current measurements. Accelerator voltage traces were measured directly at the ion source, and beam energy was propagated forward in time using the time of flight for ions of measured energy and species. We measured the ion species with time of flight evaluation of the Faraday cup data, and determined that the ion beam (using nitrogen gas in the MAP ion source) was composed of N^+, N^{++}, and H^+ in the approximate fraction of 55%, 35%, and 10% respectively. The ratio of these species is dependent on the detailed plasma and beam extraction dynamics of the ion source, and may vary by as much as a factor of two over the range of operating parameters for our MAP ion source.

We are able to measure the onset time of surface melt and the resolidification time with nanosecond measurement accuracy. These measurements allow us to conclusively demonstrate the melt-resolidification cycle, and quantitatively compare experiment and theoretical results. Figure 8 presents experimental data with silicon melt duration measurements for a wide variety of energy densities and accelerating voltage profiles. Also shown are the simulation results for those tests. As can be seen from this graph, good agreement is obtained for all these tests, within the experimental uncertainty of the fluence values. This confirms our ability to model the behavior of the ion beam in the case of materials with extremely well known thermal properties. At high fluence, above about 2.3 J/cm^2 the experimental values begin to deviate, showing a longer melt duration than predicted by the code. This is the energy range in which ablation begins, and this effect is not rigorously included in the present model.

Also implicit in these results is a confirmation of the beam energy density measurement itself. The energy calibration from quantitative Faraday cup appears to be a very good means of measuring beam fluence, integrating the ion current as measured from Faraday cup signals, and multiplying that by the accelerating voltage. Figure 9 gives results from a number of simulations in which the details of the ion species, and the temporal variation in voltage and current are varied. We find that the parameter of most relevance is the total fluence. Less important, within the error bars of present experimental uncertainty, is the detailed waveform. This is intuitively expected because the beam pulse duration is about 100 ns, very short compared to the melt duration of several microseconds. Melt duration is not significantly influenced by specific ion species distribution, again because the longer time scale of the melt process averages out the short time scale of the ion deposition profiles. The experimental variation of the ion species fraction gave a maximum melt depth variation of +/- 0.1 μm at the low fluences of this experiment.

The energy deposition distribution is fixed by the ion species, through a combination of the depth of penetration, the fluence, and the time of flight. Figure 10 shows the ion profiles, calculated from voltage waveforms and Faraday cup data, and time shifted by the transport time for the given ion at the measured voltage. The first 80 ns of the pulse is dominated by protons, which travel fastest, and have the deepest penetration. This establishes an initially low thermal gradient through the first few microns of depth. The

next 60 nanoseconds is dominated by the N^{++} beam, with moderately deep penetration. The last 80-100 ns produces the strongest surface heating from the primary N^{+} ions. In this final phase, it appears that most of the surface ablation occurs, when total energy density exceeds about 2 J/cm^2 . Surface ablation observations were made with reflectance data collected without a laser interference filter, which allowed additional "white" light observed during onset, coming from the heated substrate itself. The onset of this ablation signal is first seen at about 1.6 J/cm^2 . The magnitude of the ablation signature increases with energy density, becoming significant over 2 J/cm^2 and melt duration of more than 2.5 μs. The onset of ablation coincides with the tail of the ion pulse, corresponding with surface energy deposition from the heavier nitrogen ions. Visual roughening of the silicon surface was observed for melt durations over 2 μs.

Mass diffusion from the heated surface into the bulk material was measured with samples that were implanted with a trace amount of Arsenic, which allowed concentration measurement in depth, as a function of energy density. The Arsenic was implanted at 100 KeV into silicon samples to 8E15 $atoms/cm^3$ concentration, as shown in Figure 11a, b. Figure 11c shows measurement of the effective diffusion depth as a function of energy. The linear fit to these data gives an effective diffusivity of 2.19 x 10^{-4} cm^2 /s, in good agreement with the accepted value of 2.32 x 10^{-4} cm^2 /s for laser melting. This agreement with the laser melt data implies that the melt pool formed in the pulsed ion beam process in basically quiescent, and not dominated by convective mixing on the 2.5 μs time scale of the melt duration.

In summary, these results show that:

1. Pulsed ion beam permits direct quantitative determination of fluence – with no adjustable absorption factors needed for simulation matching.
2. Precise beam profiles do not strongly influence the melt history for moderate melts - variations in beam are not important, with only the average fluence being important.
3. In Si, melt durations of 2 μs are feasible without sample damage; durations up to 5 μs are possible if surface roughening can be tolerated.
4. Even for long melt durations, effective liquid phase diffusivity is equivalent to short duration measurements from laser processing.
5. Measured surface melt durations match extremely well with numerical simulations.
6. At high fluences, experimental duration is longer than predicated -- origin unknown presently.
7. Quantitative simulations of pulsed ion-beam processing are reliable.
8. We can use simulations to model metal alloys where direct measurements are not presently possible.

Reflectance Measurements

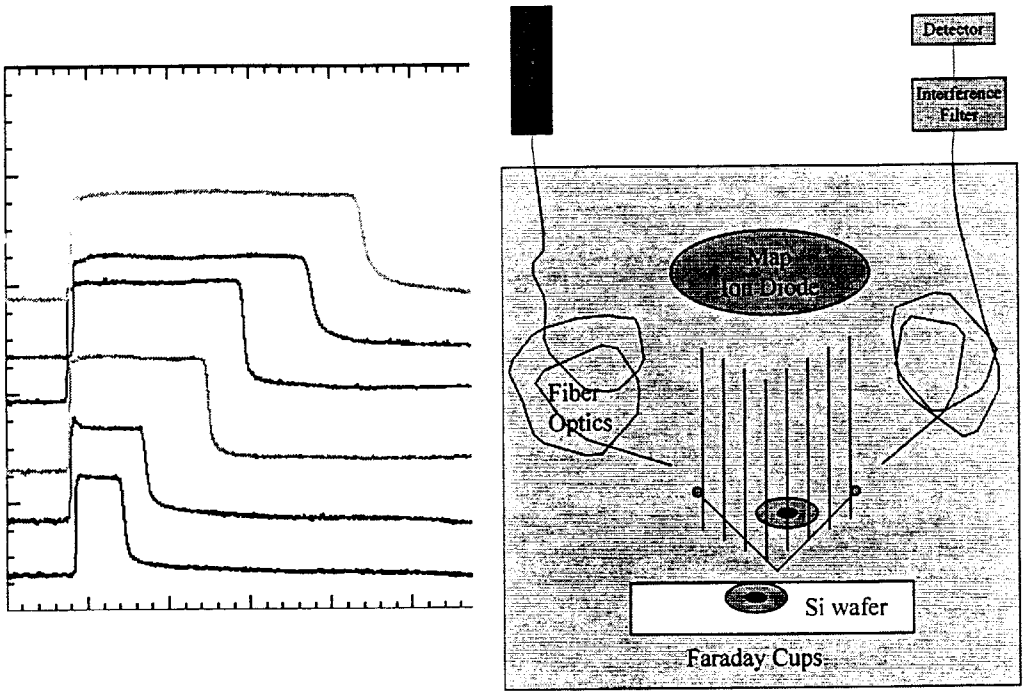

Figure 7. Arrangement for the laser reflectometry experiment.

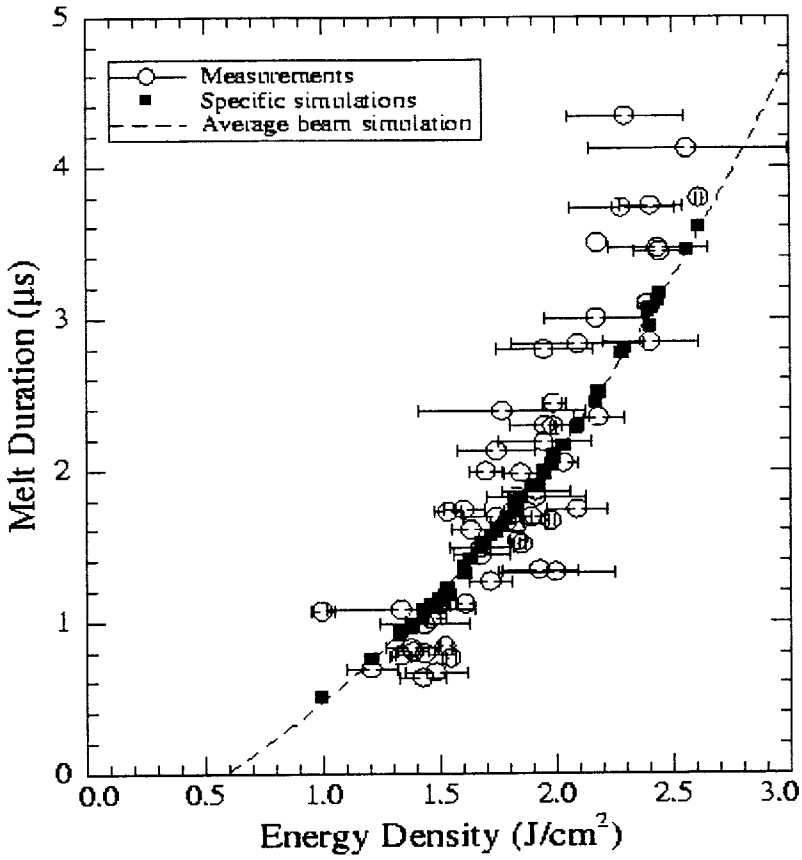

Figure 8. Melt duration experimental data for silicon, compared with simulations.

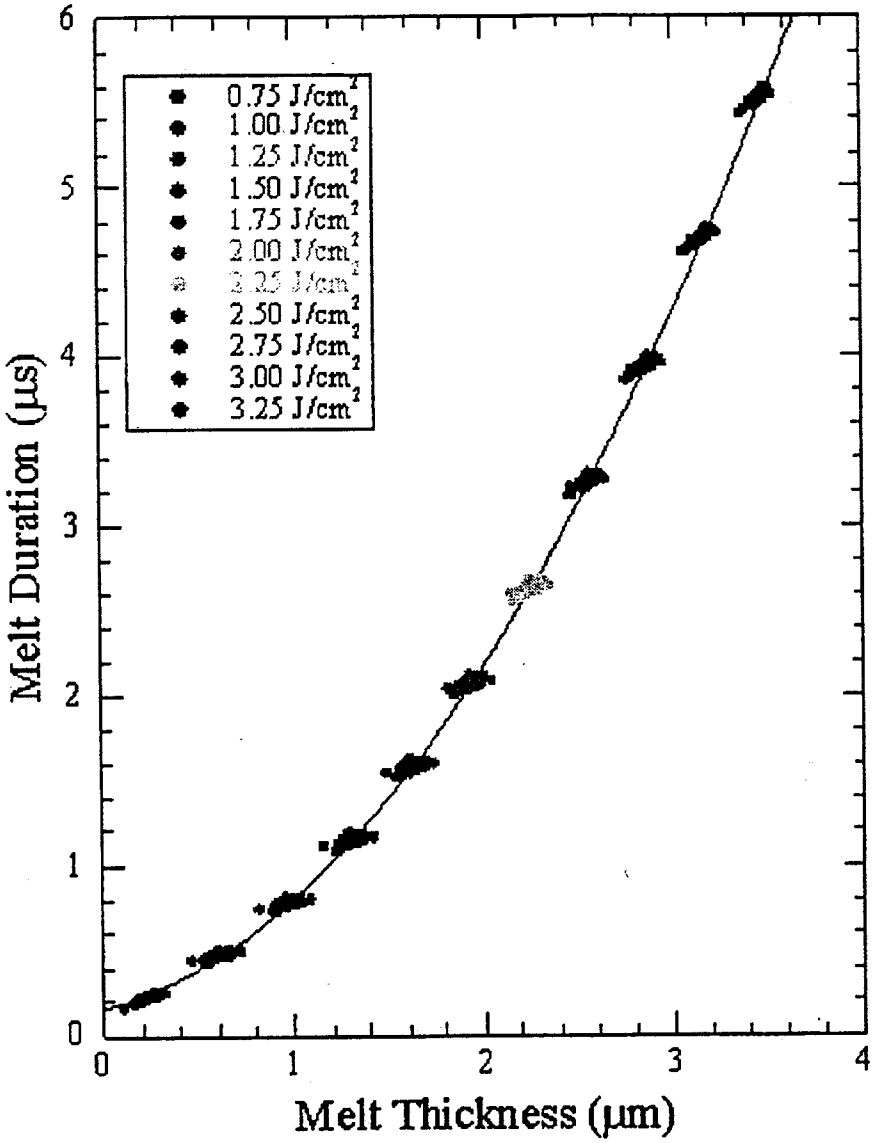

Figure 9. Melt duration simulations for silicon, comparing various beam profiles and conditions.

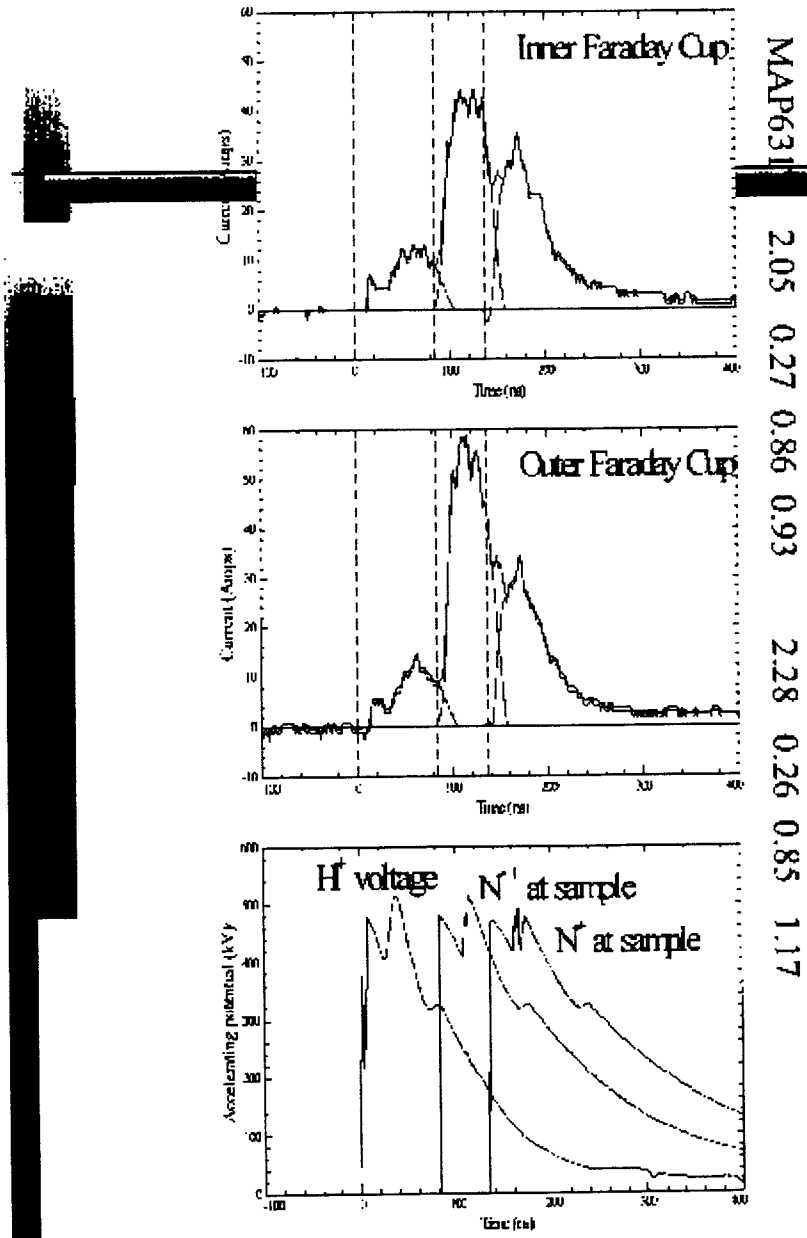

Figure 10. Ion Species Extraction

Figure 10. Ion Species Extraction showing arrival times and ion species profiles.

Arsenic Diffusion Measurements

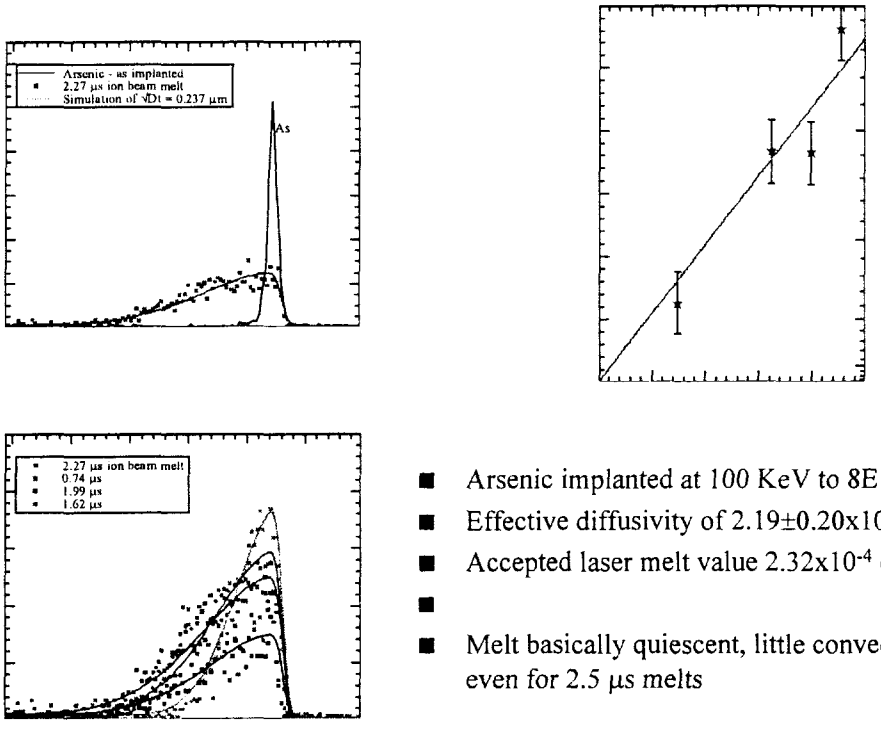

- Arsenic implanted at 100 KeV to 8E15 dose
- Effective diffusivity of $2.19\pm0.20\times10^{-4}$ cm^2/s
- Accepted laser melt value 2.32×10^{-4} cm^2/s
-
- Melt basically quiescent, little convective mixing even for 2.5 μs melts

Figure 11. Diffusivity experiment using Silicon with implanted arsenic.

3.3 Surface Alloying and Mixing with High Intensity Ion Beams

We have completed a number of experiments that use the ion beam to mix a thin-film overcoat metallic layer into Fe, Ti, and Al substrates. With respect to Al alloys, it is well known that certain transition metals (Ti, V, Cr, Zr, Nb, Hf, Ta) can improve corrosion resistance, but are almost insoluble in Al under equilibrium conditions. The IBEST rapid heating cycle can be expected to yield a metastable solid solution of the bulk substrate phase at atomic concentrations above these solubility limits. In addition, it is desirable to limit the number of second-phase particles in the resulting alloy, since these can act as initiation sites for corrosion. For these experiments, the coatings have been sputter-deposited either in pure form or as a "co-sputtered" alloy. In the latter case, two sputter guns are operated simultaneously, one emitting the candidate coating, the other the elemental substrate metal in a predetermined ratio. We are also investigating other less costly methods of applying the thin-film coating.

The advantage of surface alloying over surface modification alone is that the mixing of a previously deposited layer into a bulk substrate can produce a novel surface alloy with properties superior to those of the substrate. The advantage of surface alloying over standard thin-film deposition alone is that the beam processing grades the coating into the substrate, effectively eliminating the interface between coating and substrate. Thus processing with high-power ion beams can be superior to sputter-deposited films alone,

because of the adhesion problem associated with the high stresses inherent in such films, which limit their thickness to ~ 0.5 μm. Successful mixing should result in an inherently stronger bond with the underlying substrate, and potentially extend the surface composition and properties to the maximum melt depth attained during the power pulse. For Al substrates, this can be as much as 5-7 μm.

We have tested Al alloys overcoated with all the elements listed above, where the overlayer thickness ranges from 300 Å to 2 μm. RBS studies indicate that in the case of a 300 Å Cr layer on Al, the Cr migrated into the Al at a 2 at% concentration to a depth of 8000 Å, and may have diffused as much as 1-2 μm further, or most of the distance that the Al was melted during the pulse (estimated at 5 μm). X-Ray Diffraction measurements are consistent with a supersaturated solution of 2 at% Cr in Al, although since at this concentration level the measurements are insensitive to Cr precipitates, further tests are necessary with thicker Cr layers to verify the lack of second-phase particles. Electrochemical impedance tests in a NaCl solution show the Cr-Al sample to be superior to either untreated or beam-treated Al alloy in corrosion resistance. These results are discussed in more detail in the next section.

We are also experimenting with overcoats on Al to improve surface hardness. It is known that Si, when added to Al, either in precipitate form (large inclusions) or in a finely distributed matrix, can lead to surface hardening and increased wear resistance. We have treated Al with Al-Si overlayers. Preliminary nano-indentation measurements indicate a significant IBEST-induced hardening of the Al by up to 300%. Surface wear tests of these samples are discussed in Section 5.2 below.

We have also produced metastable alloy formation with Fe and Ti alloys. Combined RBS and X-Ray diffraction measurements indicate mixing of Ta into Fe with a surface concentration of 30 at%, with no second-phase particles indicated. Pd and Pt have diffused into Ti substrates with surface concentrations up to 15 and 30 at%, respectively. Several Pt/Ti samples, when subjected to Anodic Polarization in an air-equilibrated 1.0M NaBr solution, and unlike untreated Ti, exhibited an active-passive transition similar to that observed for stainless steel. This indicates an increased level of corrosion resistance. One Pt/Ti sample, with 1600 Å Pt overcoat, resisted stable pit formation until 1.7-1.9 Vsce, compared to 0.3 Vsce for untreated Ti. X-Ray diffraction measurements indicate the presence of unknown spectral lines consistent with metastable alloy formation of coating and substrate materials.

Platinum in Ti appears to produce the best combination of corrosion resistance improvement and surface hardening in Ti. We have observed that nitrogen in the accelerated beam produced a higher degree of surface hardening than that produced with argon. This supports the hypothesis, thus far untested, that surface modification results are ion-dependent. Further surface alloying results are detailed in the sections below.

General observations are reported below for the three main classes of metallic substrates that have been studied: Al, Fe, and Ti. Selected examples of changes in properties are then given. Properties typically tested include hardness, surface roughness, durability and wear testing, and corrosion resistance. Ion beam treatment is characterized by total power density W_d (W/cm^2), which is defined by three explicitly controlled treatment parameters: 1.) ion beam energy density, E_d, 2.) pulse length, τ, and 3.) number of pulses, n. These parameters are noted where appropriate.

4.0 Surface Treatment Results for Ferrous Metals

A variety of ferrous alloys have been treated with RMR and studied including carbon steels, alloy steels, martensitic stainless steels and austenitic stainless steels. Additionally, attempts have been made to mix Cr, Ta and Rh into iron substrates. The majority of our work has focused on austenitic alloys, and they have been observed to respond favorably to ion beam treatment.

Melt depth predictions by melt code modeling agree with observed melt depths of 1.0 to 2.5 μm for ion beam treatment where $n < 25$, $E_d < 6$ J/cm^2 and $100 < \tau < 500$ ns. Ferrous materials are susceptible to microcratering, but to a lesser extent than aluminum alloys. Like aluminum alloys, there appears to be a total ion dose maximum beyond which microcratering decreases.

4.1 Corrosion Resistance Improvement of Stainless Steels

RMR tends to homogenize austenitic alloys by dispersing sulfide and carbide inclusions in the alloy. Localized corrosion resistance is dramatically improved in aqueous acid chloride environments as a result. There is evidence to suggest that a passivating thermal oxide is produced during RMR treatment. This layer has a substantial positive effect on the corrosion resistance of RMR treated austenitic alloys. Experiments have been conducted to show that Cr depleted regions formed adjacent to grain boundaries by furnace sensitization treatment are dispersed with attendant improvements in resistance to grain boundary attack.

In prior work we showed that pitting resistance of 304, 304L, 316L and 316F could be improved by ion beam treatment. In an extension of that work, we have conducted initial tests on CRES 320 to determine if the same response could be observed. Anodic polarization of CRES 320 exposed to a pH 2 H_2SO_4 plus 0.5 w/o NaCl solution was conducted. The results are summarized by the polarization curves in Figure 12. This figure shows a curve measured from a moderately treated surface and one from a nominally untreated surface. At a moderate treatment level there is substantial improvement in the pitting resistance of CRES 320. No pitting was detected up to the highest potential tested (+1.0V), and there was a slight reduction in the passive current density. Additionally, the open circuit potential was shifted in the positive direction indicating that the surface was passivated, probably by a thermal oxide produced during ion beam treatment.

We have studied passivation kinetics of RMR-treated austenitic stainless steels. Figure 13 shows a comparison of treated and untreated 304L in a 500 ppm NaCl solution. This comparison shows that the RMR treated sample passivates more rapidly and develops a more protective oxide film compared to its untreated counterpart. These data also show that resistance to pitting in chloride solutions is improved by RMR treatment.

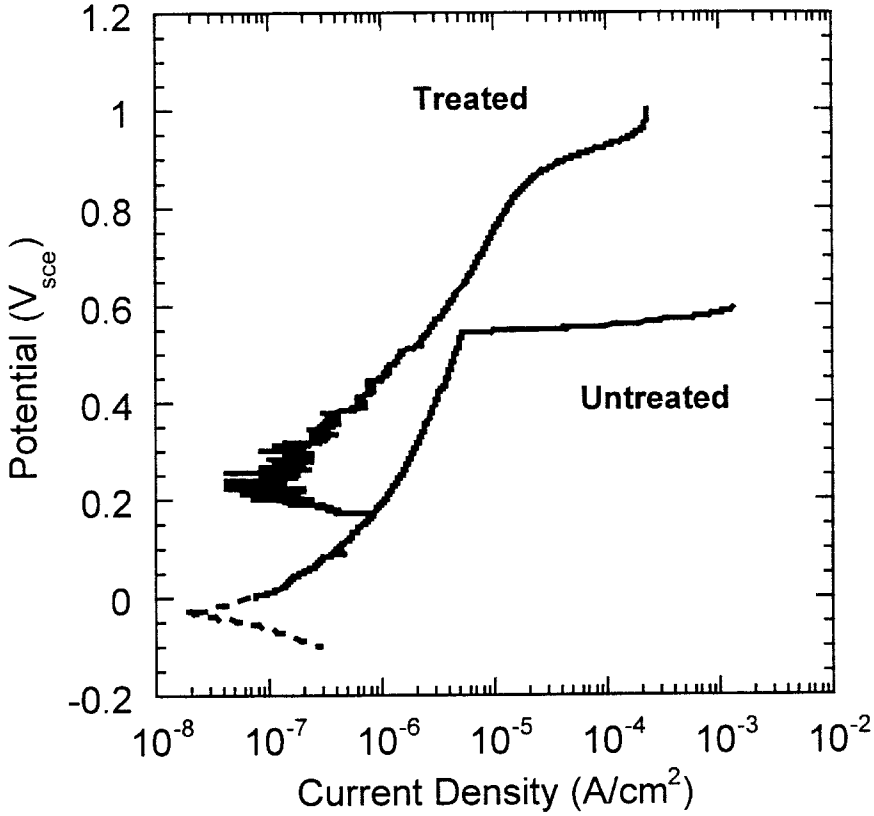

Figure 12. Anodic polarization curves for CRES 320 determined in pH 2 H_2SO_4 plus 0.5 w/o NaCl. The curves are for a nominally untreated surface and a moderately treated surface. These data show substantial improvement in pitting resistance for the moderately treated surface.

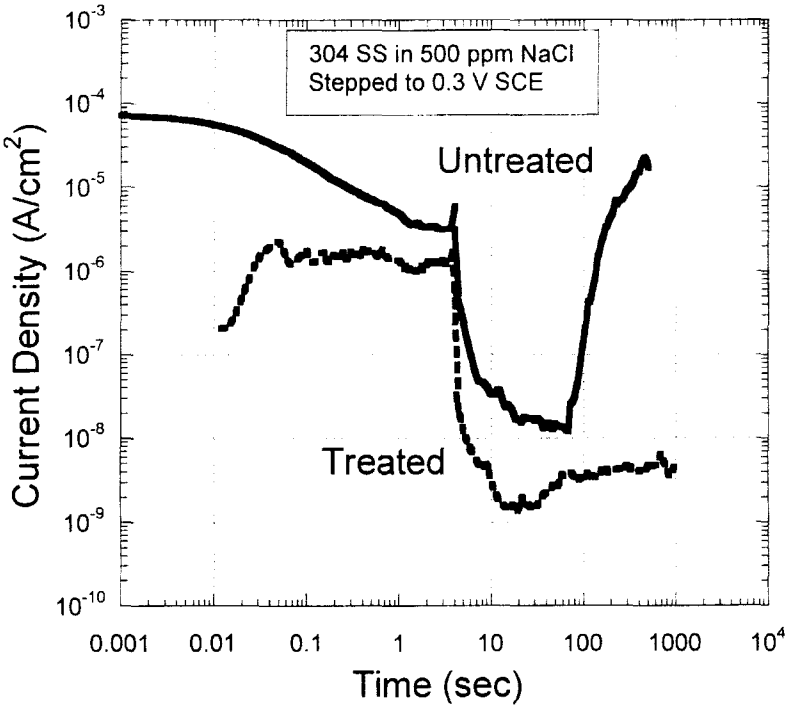

Figure 13. Passivation transients (current decay at constant potential) for treated and untreated type 304 stainless steel. The treated sample exhibited lower currents throughout and did not pit, even after 1000 s, while the untreated samples underwent pitting after 100 sec exposure.

Martensitic stainless steels are designed to form a martensitic structure by quenching after an austenitizing heat treatment. A subclass of these steels can be tempered by further heat treatment to optimize mechanical properties. In general, these materials are less corrosion resistant than austenitic alloys due to lower chromium contents (12 - 17%) and the presence of carbides intentionally formed by tempering. RMR ion beam treatment was attempted to dissolve carbides in 15-5 stainless (15Cr-4.5Ni-3.4Cu-0.04C) to improve localized corrosion resistance. Figure 14 shows polarization curves for treated and untreated 15-5 stainless in a 500 ppm NaCl solution. These curves show that the passive current density for RMR treated 15-5 is 1 to 2 orders of magnitude lower than its untreated counterpart. Additionally, the pitting potential of the RMR treated material is shifted in the positive direction by approximately 100 mV indicating an increased resistance to pitting.

Figure 15 illustrates that RMR treated 15-5 exhibits enhanced passivation kinetics compared to an untreated control sample. In this experiment the sample is potentiostatically polarized to +0.300 V_{sce} and the current decay is monitored. A rapidly decaying current indicates formation of a protective passive film that is not interrupted by the presence of defects at second phase particles. The RMR treated sample exhibits a much lower current density for the entire duration of the experiment indicating the presence of an excellent passivating film.

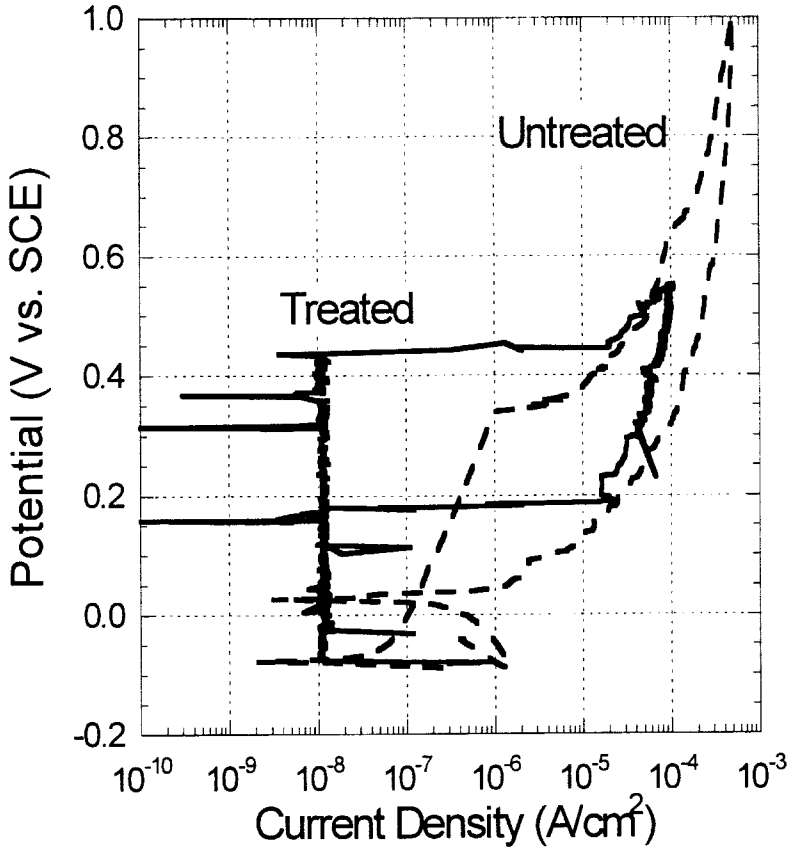

Figure 14. Polarization curves for treated and untreated 15-5 stainless steel. Both exhibit pitting, but the treated sample resists pitting to higher potentials. In addition, the passive current density for the treated sample is up to 2 orders of magnitude lower than the untreated alloy.

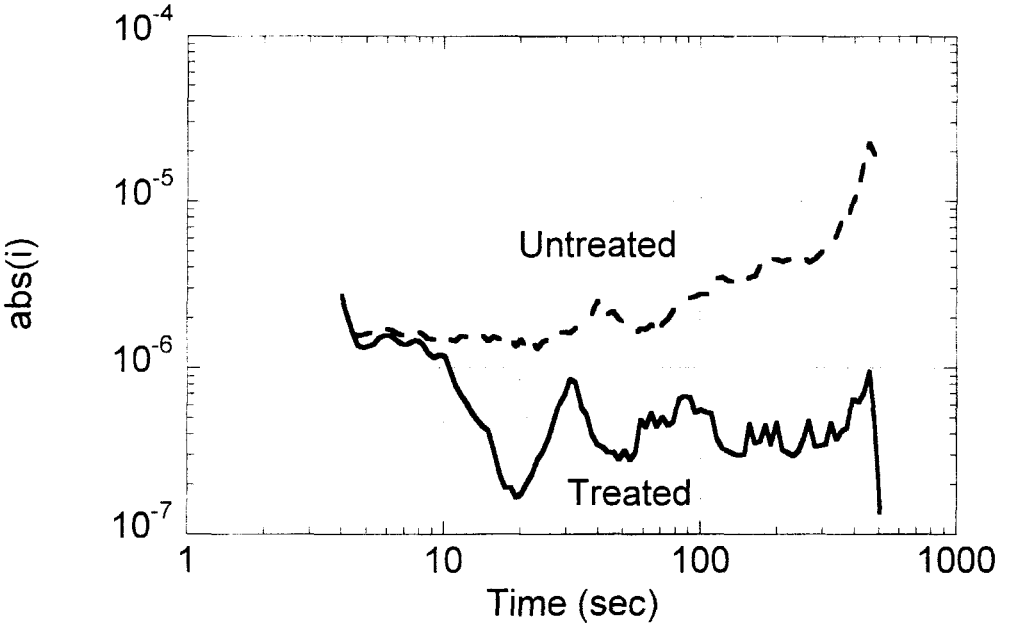

Figure 15. Passivation transients (current decay at constant potential) for treated and untreated type 15-5 stainless steel. The treated sample exhibits lower passive currents and an increased resistance to pitting.

4.2 Hardening of Stainless Steels

Single pulse RMR treatment has been observed to induce hardening in AISI 304L (Fe-19Cr-9Ni-0.03C max). Figure 16 shows a hardness versus depth profile for a sample shown in the optical micrographs on the right, where the bulk hardness value is approximately 200 units. The micrographs show shear banding, visible as sets of parallel lines, and twinning up to 80 μm below the melted region. This result is significant because it demonstrates the ability to induce changes in materials properties at depths far beyond the ion or melt range. Although our deep treatment results are not very consistent, Russian experiments also have shown this deep hardening effect with electron beams, and their experiments are more repeatable (Ref. 32). This mechanism is induced only when the pulsed power density is sufficient to induce ablation. Two mechanisms have been proposed to account for hardening in depth. In the first mechanism, hardening is produced by a stress wave that forms as the solid material just below the melted region expands and contracts according to the coefficient of thermal expansion. If the stress wave exceeds the yield stress then hardening will occur. In the second mechanism, a shock wave propagates through the material due to a recoil pulse that is generated as gaseous metal expands away from the treated surface.

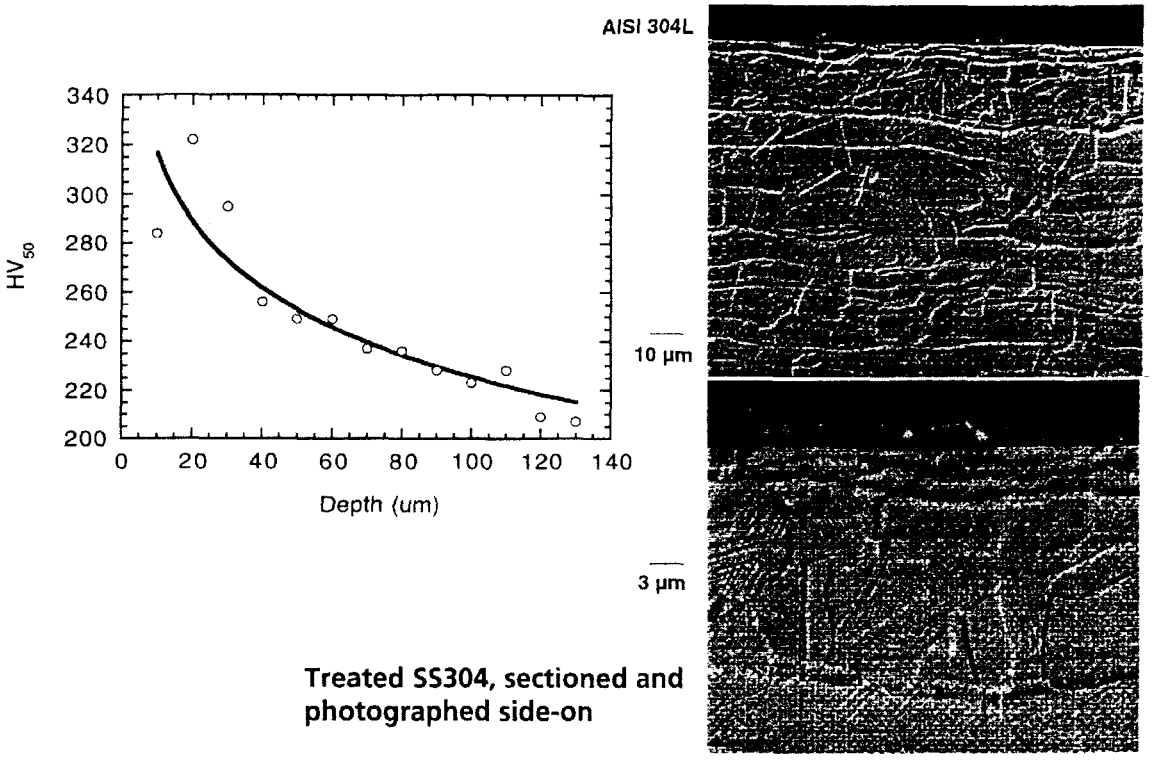

Figure 16. A plot of Vickers microhardness versus depth (taken with a 50 g load) in RMR treated AISI 304L which shows a hardening effect to depths far beyond the melted region. Optical micrographs of the sample show the 2 μ thick melted region and shear banding and twinning within grains.

Untreated and RMR treated martensitic stainless steel 440C (Fe-17Cr-1C) samples were subjected to pin-on-disk wear testing. Prior to treatment the 440C samples were heat treated , quenched, and tempered for maximum hardness followed by polishing to an average surface roughness, R_a of 20 nm. The counterface material used was an untreated 440C steel pin. The tests were run with a 1/16-inch diameter 440C steel pin at a contact pressure of 1.3 GPa under ambient laboratory conditions. Figure 17 shows a plot of the coefficient of friction as a function of the number of wear cycles for treated and untreated samples. The treated sample maintains a significantly lower friction coefficient than the untreated sample. Figure 18 shows a series of scanning electron micrographs showing wear traces formed on the samples during testing. The untreated surfaces showed evidence of substantial wear compared to the RMR treated samples. Mechanistically, the friction behavior of the control sample is typical of clean, unlubricated steel in contact. An abrasive wear mechanism is operative early in sliding, where the material removal rate is slow and debris is in the form of fine oxidized particles. At this contact stress a rapid transition to an adhesive wear mode occurs, characterized by welding at asperity contacts and transfer of material from one body to the other. The wear rate increases dramatically at this point, as does the surface roughness. A short period of low sliding friction gives way to a rapid increase in friction coefficient to greater than 0.5 and rapid wear. The treated surface shows a more gradual change in friction, which suggests suppression of the usual asperity junction growth processes. This may be the result of higher flow stress in the treated layer. Inspection of the 440C pins used as counterfaces shows that the apparent wear rate of the pin surface exceeded the wear rate of the RMR surface. When the experiment was repeated using silicon nitride balls as the counterface, we again found more wear occurring on the ball than the RMR 440C.

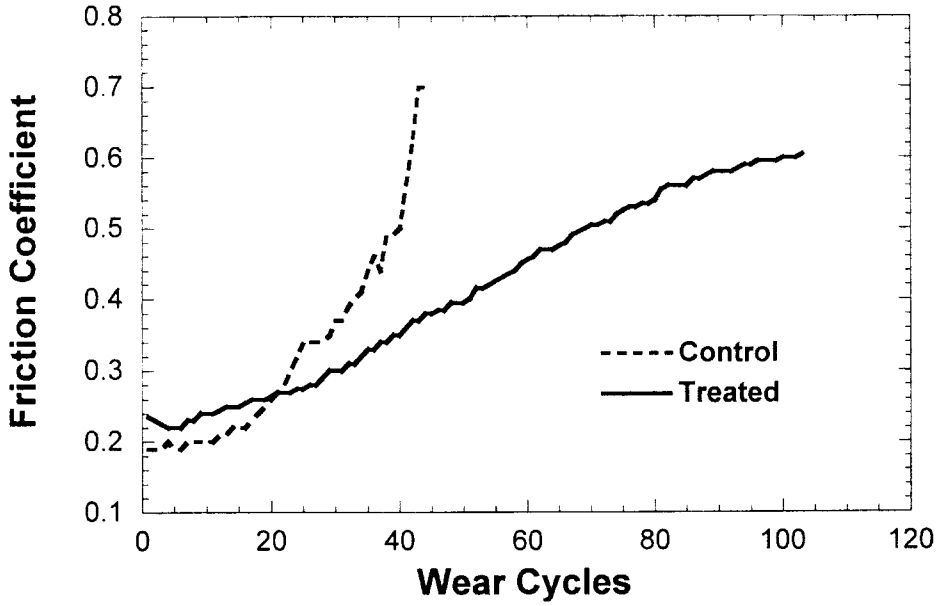

Figure 17. Variation of the coefficient of friction with increasing number of wear cycles in the pin on disk test indicating improved wear resistance for the RMR treated sample of 440C stainless steel.

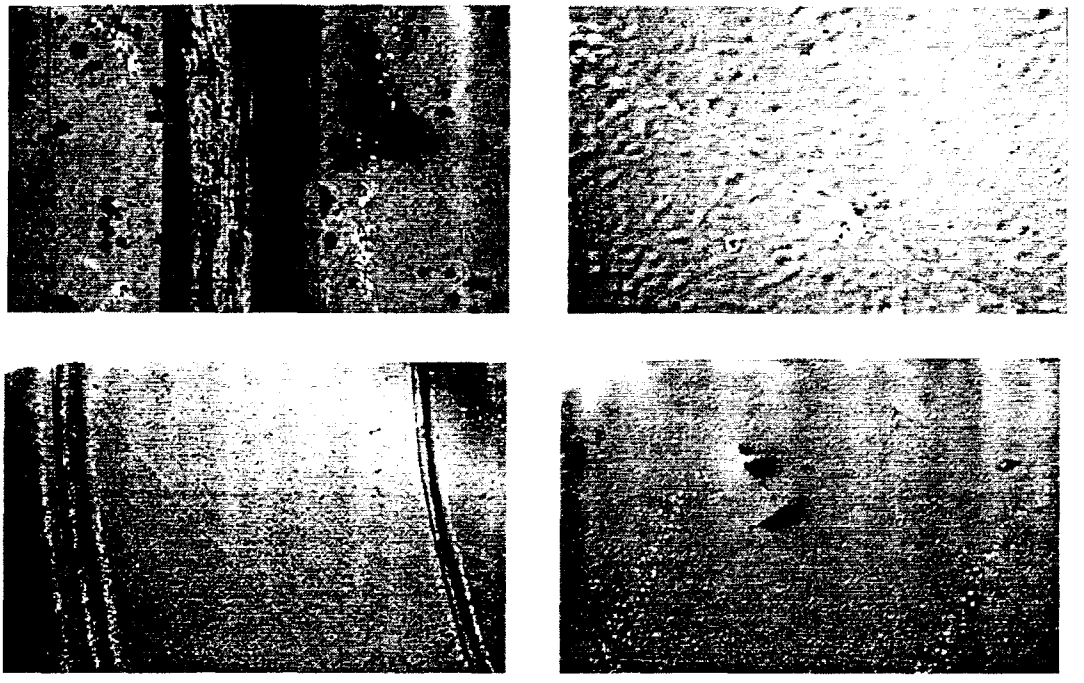

10μm/100 μm
(upper)/(lower)

Figure 18. Scanning electron micrographs of wear traces from pin on disk tests for untreated (left) and RMR treated (right) 440C martensitic stainless steel samples. The wear traces for the RMR treated samples are barely visible indicating improved wear resistance.

The cross-section of treated 440C, as shown in Figure 19 indicates that the depth of the melted layer is approximately 2.5 μm. The hardness of the treated layer has been measured by nanoindentation with a load of 0.3 g. Since the depth of the indentations were about 200 nm into a 2.5 micron treated layer, the measurement reflects the hardness of the treated layer and not the underlying substrate. The relative hardness of treated 440C as a function of treatment fluence is plotted in Figure 20. The results are compared with a measured hardness of 1.2 GPa for an untreated, polished 440C control sample. The hardness is improved by a factor of 5 for the sample treated with 1 pulse at 4 J/cm^2. The error bars on the hardness values are given by the standard deviation of the results. The increase in spread of the hardness values with increasing fluence is due to the roughening of the surface caused by RMR. Nanoindentation and Knoop microhardness testing on the treated cross section indicates that hardening is confined to the treated layer.

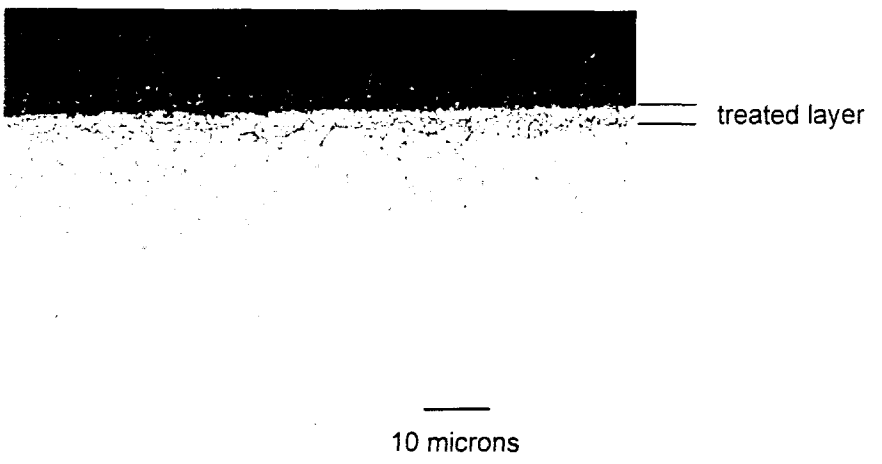

Figure 19. The depth of the treated layer in 440C steel is approximately 2.5 μm.

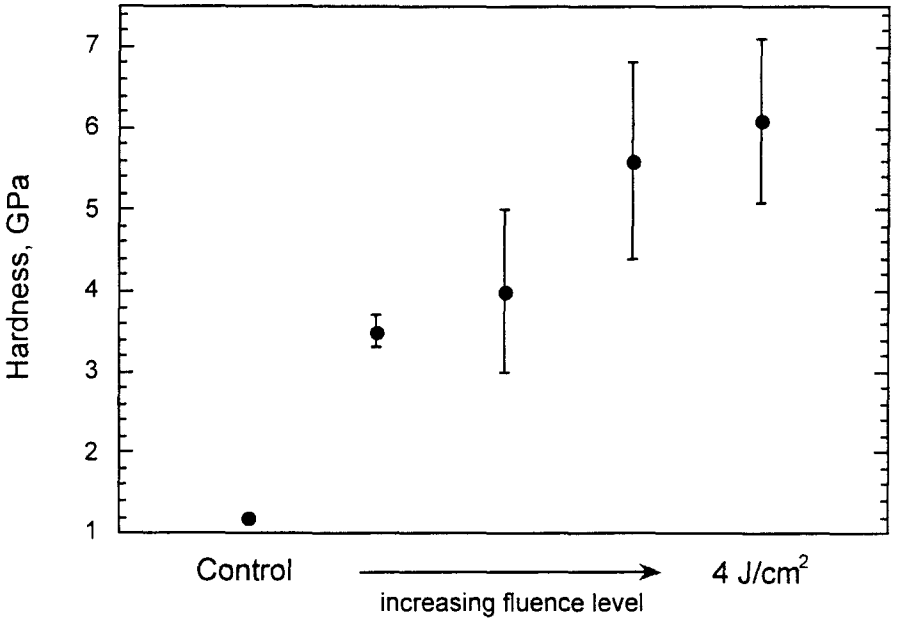

Figure 20. The hardness of 440C steel can be increased by a factor of 5 by RMR. Hardness increases with the fluence level of the treatment. The sample at the second lowest fluence received 15 shots and the others received 1 shot. Hardness values are relative.

Figure 21 shows SEM images of both the untreated and treated 440C surfaces. The polished, untreated surface shows second phase particles with an average diameter of 0.9 microns. The surface after treatment shows a martensitic structure. Second phase particles are finely dispersed in the treated surface and are not visible in SEM images. Small dark areas on the treated surface correspond to holes with an average

diameter of 0.5 microns. Depth profiling using SIMS (Secondary Ion Mass Spectrometry) shows that there is no redistribution of impurities within the treated layer.

Microcratering is observed on the treated 440C surfaces. Craters have a 1 micron high lip around the edges and a 1 micron depression in the center. The density of craters on the treated 440C surface (5 pulses @ 5 J/cm^2) is estimated at 15-30 craters/mm^2, and the craters range in diameter from 20-200 microns. The smaller, somewhat elongated holes mentioned previously are at least 0.8 micron in depth and have a density of ~900 holes/ mm^2. The mechanism causing the formation of the holes in the RMR layer is not known, but the cause may be related to residual stress in the melted layer. Treatment of thin steel samples causes the samples to curl upward indicating a tensile residual stress produced by RMR.

In addition to pin-on-disk wear testing, treated 440C samples have been wear tested with a linear, reciprocating tribometer which allows the examination of smaller, more uniformly treated areas. In these tests the counterface was an untreated 1/16-inch 440C ball with a 35 g load. The length of the wear tracks was 4 mm. In the results, shown in Fig. 22(a), RMR 440C consistently shows greater durability than the untreated metal, as indicated by the number of wear cycles before a rise in the friction coefficient. Failure is defined as occurring at the point when a friction coefficient of 0.5 is reached. The large variation in the number of cycles until failure for the treated material is believed to be caused by the roughness of the RMR sample and the small size of the tested area. Additional 440C samples were treated at a later time and also tested with the reciprocating tribometer. The wear results from the second set of samples, plotted in Fig. 22(b), are nearly identical to the first set of samples.

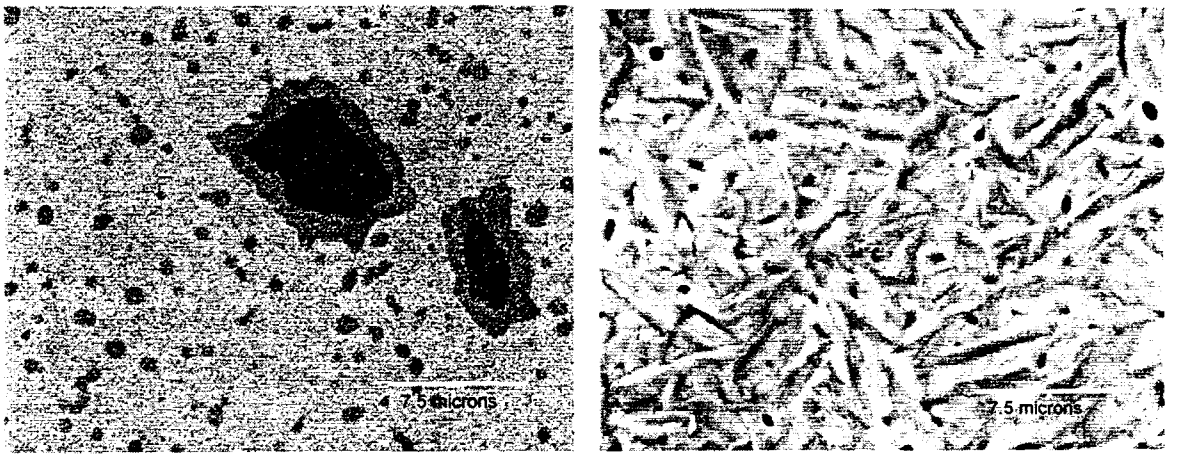

Figure 21. (a) SEM image showing the untreated 440C surface and the size of second phase particles. (b) An SEM image of the martensitic 440C surface after treatment. The dark areas are holes.

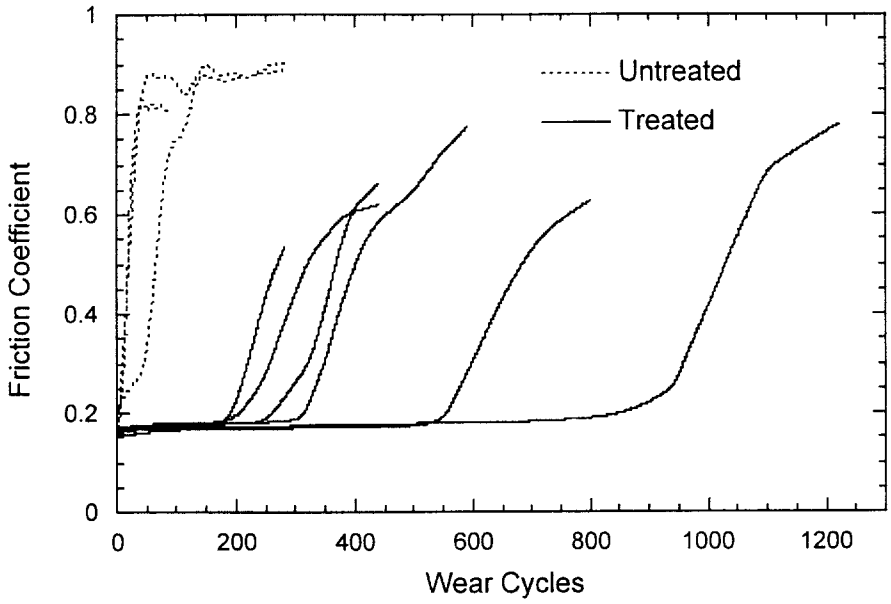

(a)

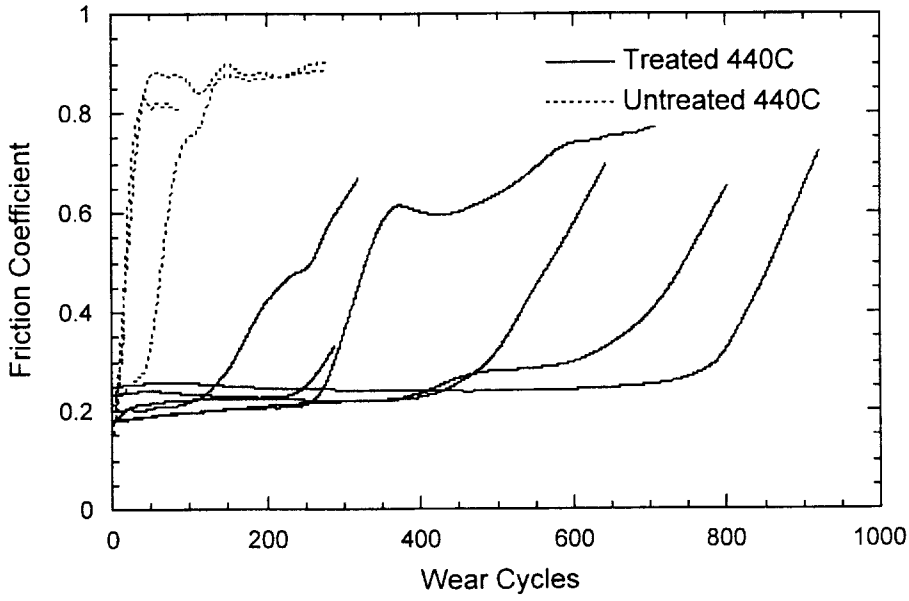

(b)

Figure 22. Wear test results for treated 440C steel samples. Samples tested in (a) and (b) were treated with the flashover diode at different times with nearly identical results.

4.3 Surface Alloying of Ferrous alloys

Fe samples were prepared by sputter deposition of a Cr layer. After beam treatment, a surface alloy is created that is somewhat similar to stainless steel, although austenitic stainless steels contain significant amounts of Ni in addition to the Fe and Cr. Corrosion tests were performed in a solution containing .005M H_2SO_4 and .001 M NaCl. Potentiodynamic polarization curves and potentiostatic current decay curves were generated for an iron blank, for the as deposited, unmixed Cr layer, and for the mixed layer at several locations on the sample.

Figure 23a shows the potentiodynamic polarization results for these samples. The Fe blank exhibits the highest currents of the group. It displays little tendency to passivate. The lowest currents were observed with the unmixed, pure Cr layer. The mixed samples, measured at five points along the sample, fall in between the two extremes, indicating that the mixing treatment improved the corrosion resistance relative to pure iron. Here, Spot A has the highest level of fluence, and Spot E the lowest. However, the corrosion resistance is inferior to that of pure Cr. There is no systematic correlation between fluence and corrosion resistance. Figure 23b presents similar data for another sample. Again, the unmixed Cr layer exhibits the highest degree of corrosion resistance. One of the mixed samples (location C) was almost identical to the unmixed layer, but the other mixed samples exhibited higher currents, indicating less of a tendency to passivate.

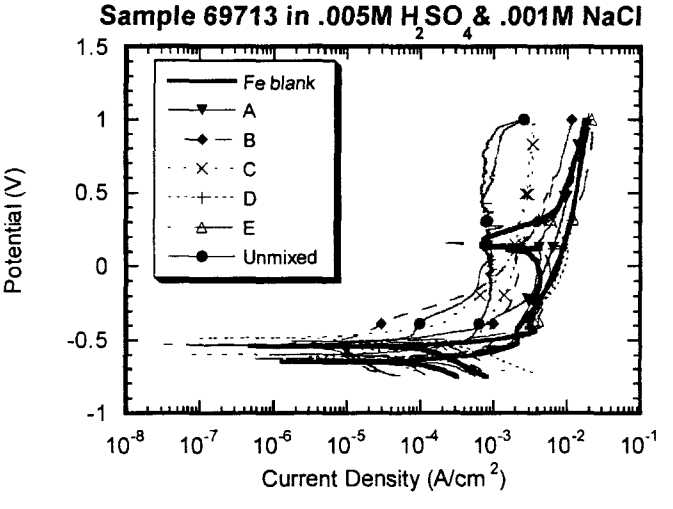

Figure 23a. Potentiodynamic polarization curves for sample 69713 in 0.005M H_2SO_4/0.001 M NaCl. Also shown for comparison is the curve for and Fe blank.

Figure 23c presents potentiostatic data for samples polarized at 0.25V (SCE), a potential about in the middle of the passive region. The Fe blank exhibits fairly high current densities, with no evidence of passivity. The currents for the unmixed Cr layer were several orders of magnitude lower. As with the polarization curves, the currents for the mixed samples were basically intermediate between the two extremes. All of the mixed samples exhibited a tendency to passivate, as evidenced by the initial current densities (two orders of magnitude below the Fe blank). However, the currents appear to be high enough that with time the treated layer is removed, exposing the Fe substrate below. This results in a response at extended times that is very similar to the that of the Fe blank. There was, however, one sample (location C) that maintained considerably lower currents. Although they were higher than for the Cr layer, they were also considerably lower than for the Fe blank or the other mixed samples.

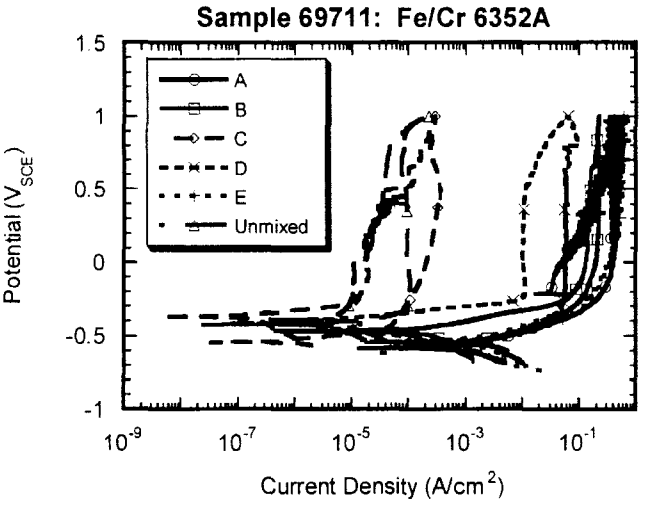

Figure 23b. Potentiodynamic polarization curves for sample 69711 in 0.005M H_2SO_4/0.001 M NaCl. Note that location C exhibited behavior similar to that of the unmixed Cr surface.

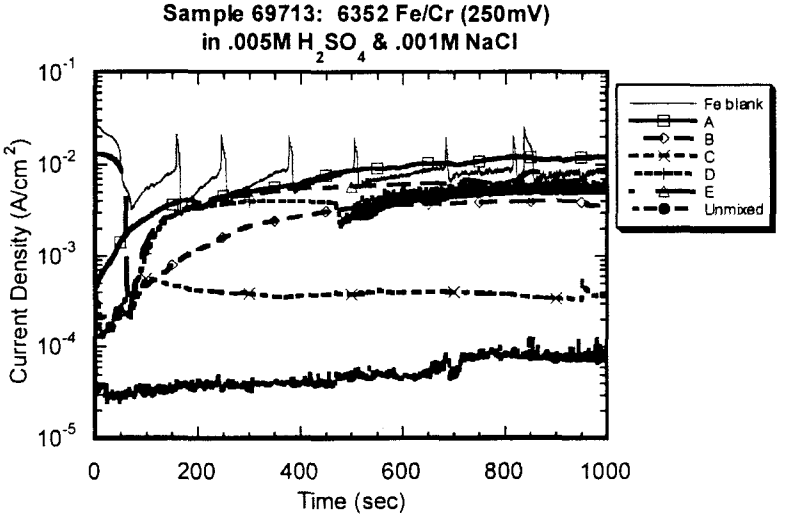

Figure 23c. Potentiostatic current decay curves for sample 69713 in 0.005M H_2SO_4/0.001 M NaCl. Samples were polarized at 0.250 V (SCE). Also shown for comparison is the curve for an unmixed (as deposited) Cr layer, and an untreated Fe (blank). The 'spiky' behavior of the Fe blank is evidently caused by alternating passivation and pitting events.

To summarize, mixing of Cr into Fe has improved corrosion resistance relative to the base Fe alloy, but only as long as the treated layer is not removed by the residual corrosion taking place. Also, the unmixed Cr thin-film coating exhibits in general superior corrosion resistance compared to the mixed layers. We plan to follow up these experiments both with thicker film layers, and with film layers containing Ni as well as Cr, to more nearly simulate standard stainless steel alloys.

5.0 Surface Treatment Results for Aluminum Alloys

Overall, aluminum and aluminum alloys have proven to be the most difficult metallic materials to treat using pulsed ion beams. In RMR treatment, impurity particles in Al alloys appear to induce microcratering under high intensity processing conditions. The microcratering can compromise any improvement in corrosion resistance. Microcratering has been observed at E_d = 2.5 J/cm^2 and is exacerbated with increasing E_d. Microcratering clearly increases with decreasing alloy purity. This effect may be the result of the significant differences in melting point of the alloying metals compared to the base aluminum. One alloying element may vaporize and create gas bubbles within the melt zone of the alloy. For instance, the melting point and vaporization point for magnesium is 648 ^{0}C and 1090 ^{0}C, aluminum is 660 ^{0}C and 2467 ^{0}C, copper is 1083 ^{0}C and 2567 ^{0}C, and chromium is 1857 ^{0}C and 2672 ^{0}C. Typical alloying concentrations are less than 1% to a few percent of these elements added to aluminum. Samples with impurity contents ranging from 1 to 100000 ppm have been prepared according to a standardized test method, and results suggest that microcratering increases to a maximum at some total ion dose, and decreases thereafter. The implication is that multipulse treatment might be used successfully to combat microcratering. Results are presented later to corroborate this notion.

Likewise, ion beam surface alloying is more problematic with aluminum. The low melting and vaporization points of aluminum compared to most of the transition metals used in deposited layers can result in ablation of the layers without mixing. Despite these difficulties, positive results have been obtained in survey experiments aimed at testing both corrosion resistance, surface hardness and smoothing of aluminum and aluminum alloys. Furthermore, there is no apparent thermophysical reason why larger improvements in these properties should not be achieved as the processing regimen matures.

5.1 Rapid Melt and Resolidification Treatment of Aluminum

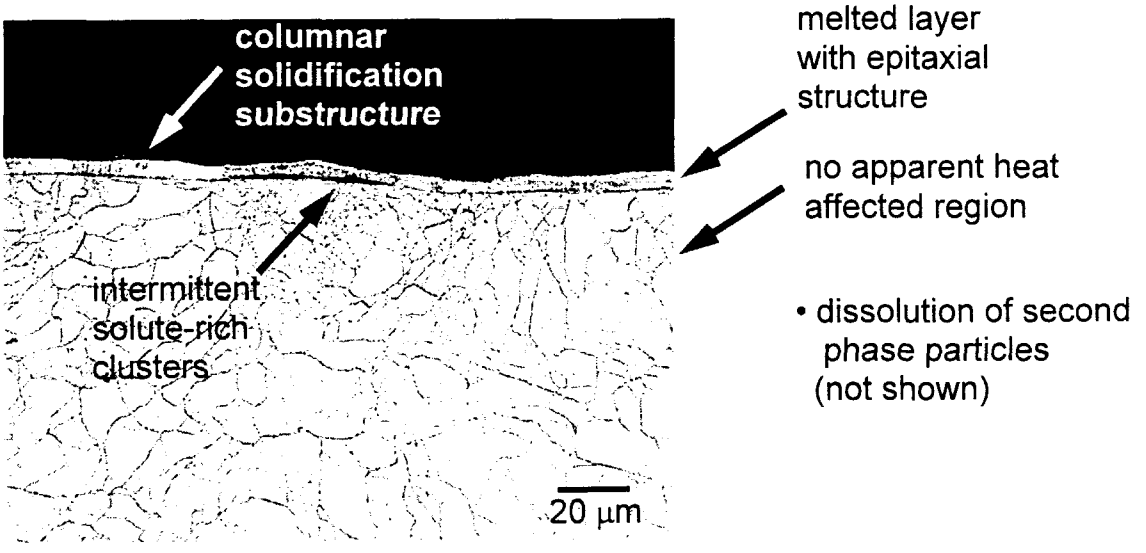

Figure 24. Optical micrograph of 7050-T73 illustrating the common attributes of RMR aluminum alloy surfaces.

The thickness of the melted layer depends directly on E_d as shown in Figure 25. This series of figures shows that the thickness of the melted region ranges from 6 μm to less than 1 μm for E_d ranging from 7.5 to 2.0 J/cm^2.

Figure 24 is an optical micrograph from a cross sectioned, polished and etched sample of RMR treated 7050-T73 (Al-6.2% Zn-2.3% Cu-2.2% Mg-0.12%Zr) that illustrates the common features of Al surfaces treated using pulsed ion beams. The figure shows a distinct melted region that exhibits an epitaxial relationship with the grain structure of the unmelted substrate. A columnar solidification substructure can also be identified. Within the melted regions second phase particles have been melted and rough surfaces are smoothed except when microcratering is induced. Occasionally solute-rich clusters are observed at the melt-substrate interface. The mechanism by which these clusters form has not been established.

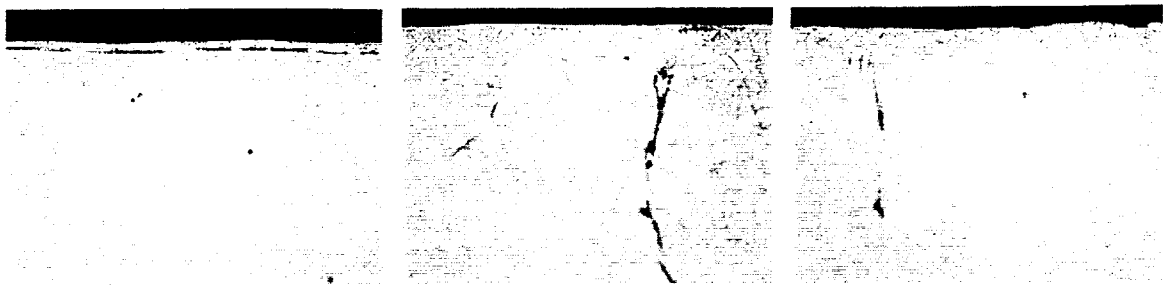

10μm

Figure 25. Optical micrographs of ion beam treated 7050-T73 showing the variation in melt depth with ion beam energy density . E_d from left to right, 6.7- 7.5 J/cm^2, 5.5 - 6.7 J/cm^2, < 2.7 J/cm^2, n = 5 , τ = 100 to 500 ns.

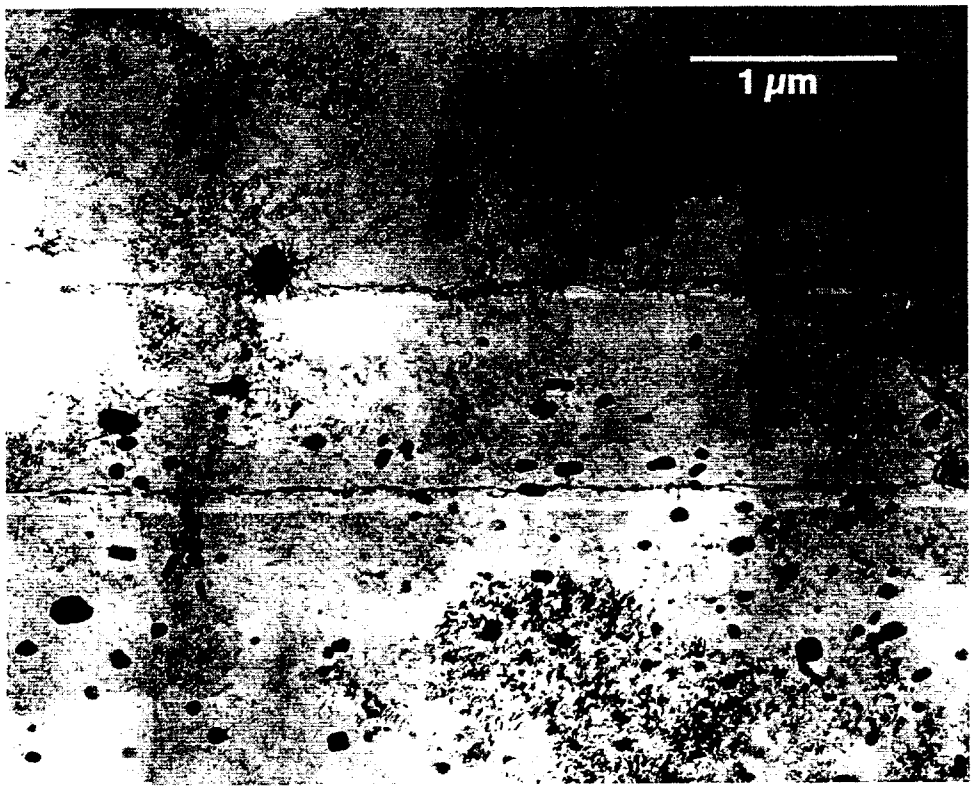

Figure 26. TEM cross section of Al 2024-T3 following ion beam treatment. Note reduced concentration of second phase particles in treated layer. The two horizontal lines in the Figure are melt/non-melt boundaries arising from shots with differing fluence levels.

Another example of the effect of ion beam treatment on the microstructure of Al alloys is shown in Figure 26. The Figure shows a TEM cross section of treated Al 2024-T3. The dark spots are second phase particles normally present in the alloy. Most of the small particles and some of the larger particles are absent from the treated zone in the upper half of the photograph, having been mixed into the bulk material.

Solute redistribution in the melted region suggests that solute mixing in metals, unlike the case with the Si study in Section 3.2, is dominated by convective forces. Figure 27 shows a series of micrographs and X-ray maps showing how solute concentrated in a dissolved intermetallic particle is redistributed after alloying at 3.5 J/cm^2. The figure in the upper left is a backscatter electron micrograph showing the treated sample in cross section. Cu, Fe, Mn rich inclusions are visible in the untreated substrate (right side of image). In the treated layer (near the black area), a bright, smeared-out region is visible. X-ray maps show that this region contains elements concentrated in inclusions (Cr and Mn) indicating that this is a dissolved particle. The breadth of this region is 2.0 to 2.5 μm. Assuming a total melt time of 5 μs (1 μs per pulse x 5 pulses) and a liquid phase diffusion coefficient of 10^{-4} cm^2/s, a diffusion path length no greater than 0.25 μm is predicted. As a result chemical diffusion alone can not account for the observed redistribution of solute. Since the redistribution is much greater than 0.25 μm, convective forces must be playing a substantial role in dispersing solute.

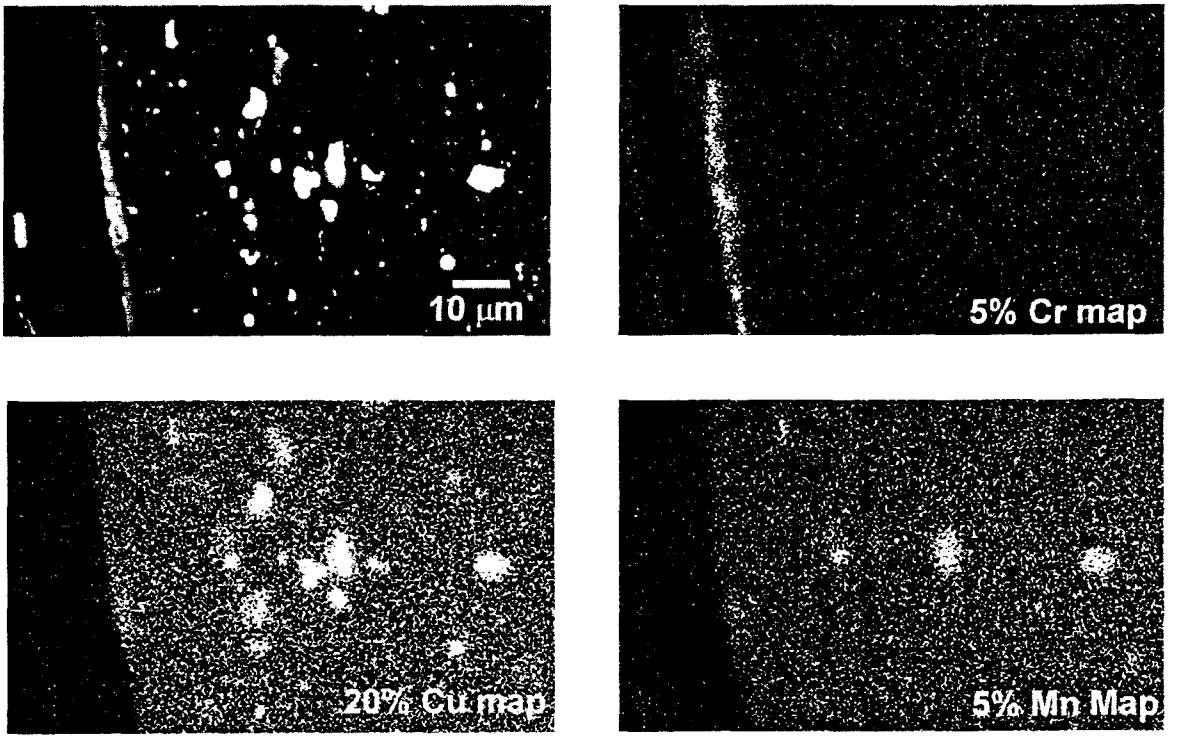

Figure 27. Backscatter electron micrograph and characteristic X-ray maps for IBM 2024-T3 with 550Å Cr showing dissolution of an Al-Cu-Fe-Mn second phase particle, and the enrichment of Cr in the solute-rich region.

5.2 Surface Alloying of Aluminum to Improve Corrosion Resistance

Surface alloying (mixing) with aluminum substrates is complicated by the relatively low melting and boiling points of aluminum. However, it appears that multiple pulse treatment can successfully produce homogeneously mixed surface layers. This is illustrated by the example in Figure 28. This figure shows two pairs of micrographs. In the left pair, n = 10 while in the right pair n = 25. The X-ray maps show the distribution of Cr in the mixed region. Cr is distributed heterogeneously in the n = 10 sample, but is much more evenly distributed in the n = 25 sample.

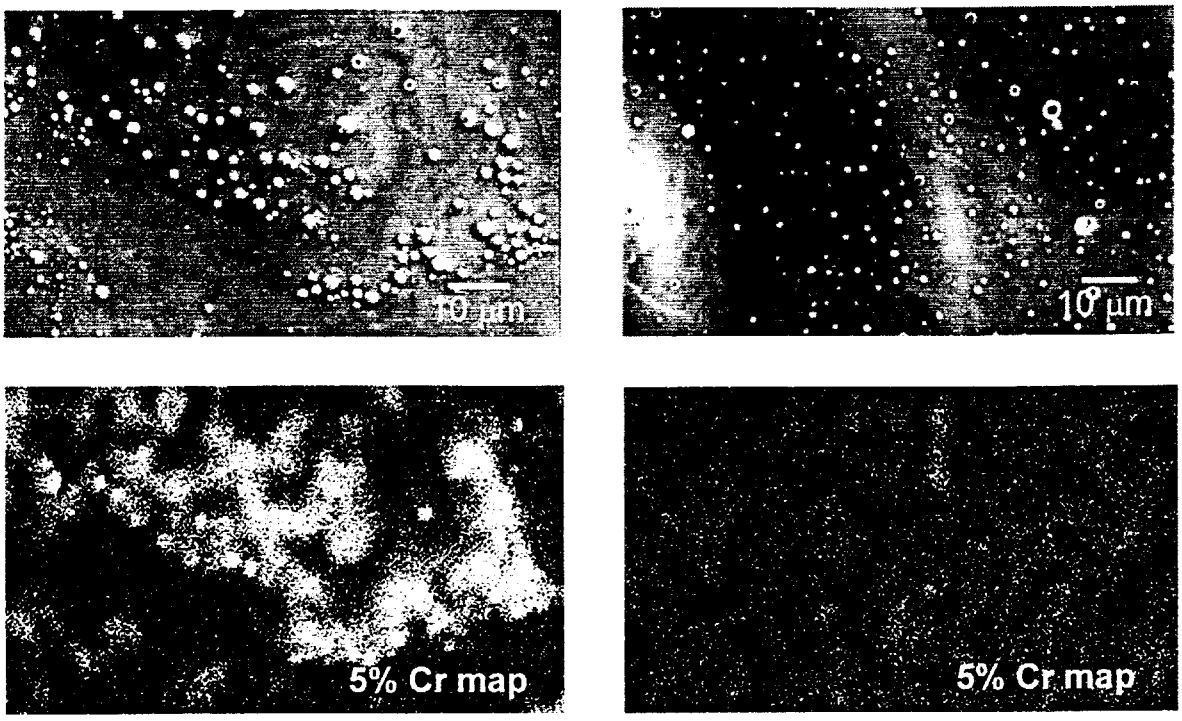

Figure 28. Backscatter electron micrographs (upper micrographs) and characteristic X-ray maps (lower micrographs) illustrate the beneficial effects of multipulse treatment on mixing of Cr into 99.999% Al. Left pair: n = 10, right pair: n = 25.

Corrosion resistance of mixed samples was assessed using electrochemical impedance spectroscopy (EIS). EIS was conducted on samples exposed to aerated 0.5 M NaCl for 24 hours. EIS scans were run immediately upon immersion in the electrolyte, and repeated at various time intervals during the 24-hour exposure. The resulting data were analyzed using an equivalent circuit model consisting of an imperfect capacitor in parallel with a resistor to model the pitting process occurring on the samples. This circuit element combination was placed in series with a resistor to account for the solution resistance. By fitting the experimental data to this circuit model, a charge transfer resistance (Rp) was obtained that is used to describe the pitting resistance of the surface exposed to the NaCl. The pitting resistance was used as the figure of merit to assess the degree of corrosion inhibition induced by IBEST treatment.

Pure Al exhibits excellent resistance to pitting attack due to the lack of second phase particles present in the metal matrix. However, the inferior mechanical properties of pure Al make it uninteresting as an engineering material. Thus, the treatment of Al alloys has focussed on imparting corrosion resistance to alloys of engineering interest. A series of elements including Re, Cr, Hf, Ta, W, and Zr was mixed into 6061 Al. The corrosion results are presented as plots of Rp values as a function of exposure time. Figures 29a and 29b show EIS results for two pure Al alloys (99.9 & 1100) and for 6061, an Al-Mg-Si alloy. In all

cases, the measured Rp values were in the $10^4 - 10^5$ range. There was essentially no change with time, indicating that the pitting behavior of the alloys did not change with time.

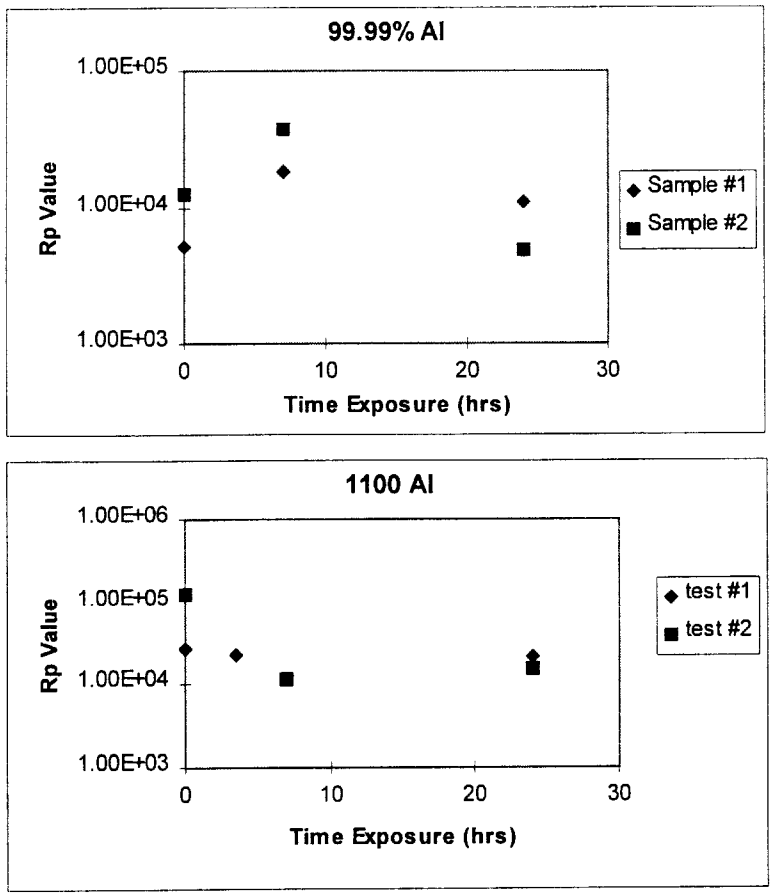

29a. EIS results for pure Al & Al 1100. Both exhibit Rp values in the $10^4 - 10^5$ range.

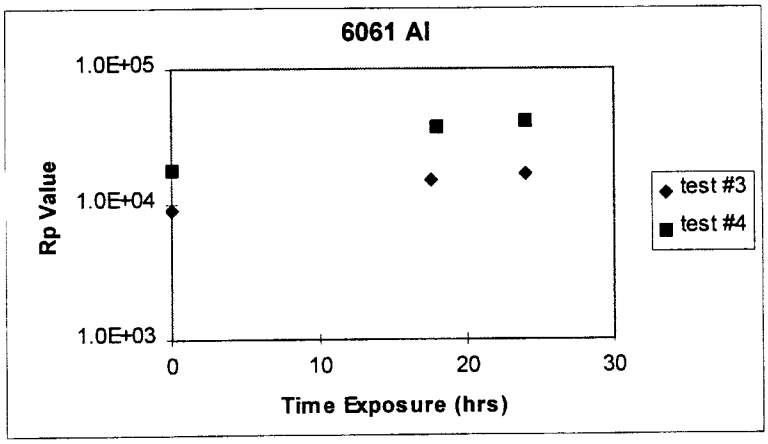

Figure 29b. EIS results for 6061 Al. Rp values are in the $10^4 - 10^5$ range.

Figure 29c presents data for 300 and 600Å of Cr mixed into 6061 Al. In Figures 29c-f, tested samples were treated as varying fluence levels ranging from lowest (Lo) to highest (Ro). The unmixed data (for the as-deposited Cr layer) show no improvement over the mixed samples, and generally exhibit lower Rp values. This is probably due to the fact that the deposited film is not thick enough to completely cover the Al, and allows the Al to contact the electrolyte through pores in the Cr layer. For both samples, there is little evidence that the mixing process has produced a more corrosion resistant surface, as the Rp values are still about 10^5. With exposure time, the Rp values decrease, indicating an increased susceptibility to pitting with increasing immersion time. Figure 29d presents results for a co-sputtered film (90:10 Al:Cr). In this case, there appears to be less of a decrease in pitting resistance with time. The as deposited surface is still inferior to the mixed surfaces in general. Some of the areas tested exhibit Rp values that are close to 10^6.

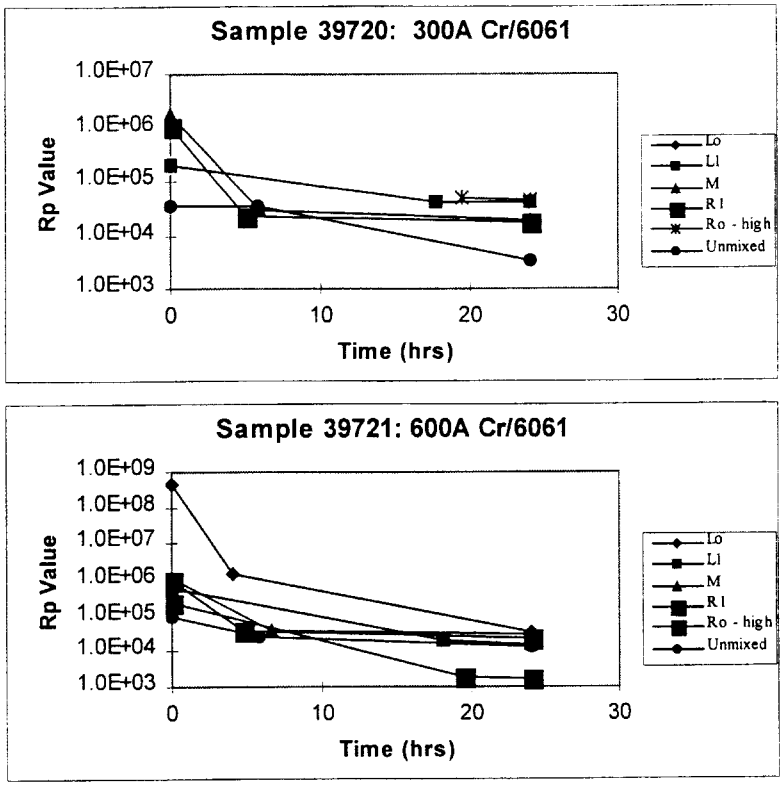

Figure 29c. EIS results for Cr mixed into 6061 Al.

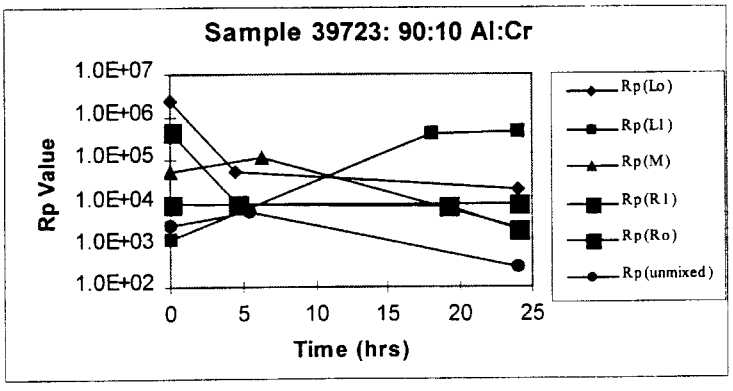

Figure 29d. EIS results for co-sputtered Cr/Al films mixed into 6061 Al.

Most of the elements, when added to the 6061 Al, produced results similar to the Cr results. The most notable results were obtained from surface produced by mixing Hf into 6061 Al. The results are presented in Figure 29e. Rp values for some of the locations tested were greater than 10^6, with little or no decrease observed with increasing exposure time. There is no apparent effect of thickness as the thick layer (4375 A) produced very similar results to the thin sample (520A). In one instance, exceptional corrosion resistance was observed on an Al-Hf sample. The results are shown in Figure 29f. In this case, Rp values of almost 10^8 were observed.

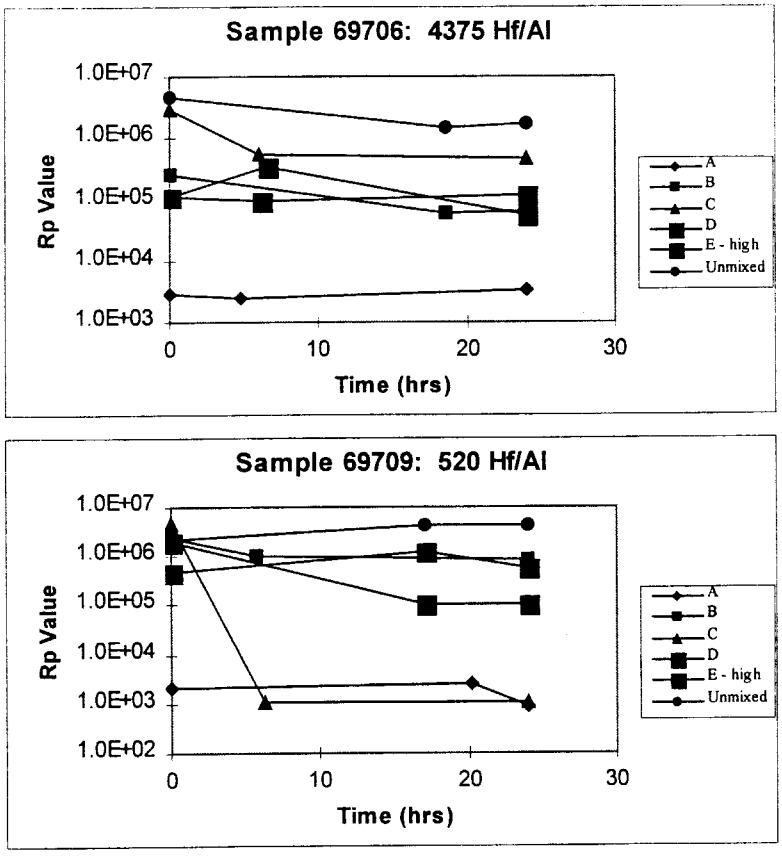

Figure 29e. EIS results for Hf films mixed into 6061 Al.

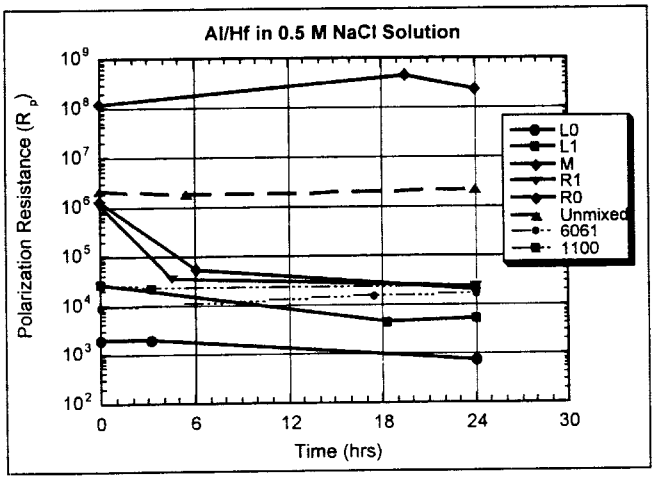

Figure 29f. EIS results for Hf films mixed into 6061 Al.

5.3 Surface Alloying of Aluminum to Improve Surface Hardness

The surface alloying of Al with Si has been investigated with the intention of creating hard, wear-resistant surfaces on aluminum. Al (6061-T6) samples with overlayers of either 80% Al - 20% Si or 60% Al - 40% Si have been treated with both the flashover diode and the MAP diode with nitrogen gas. The samples were arranged in a radial pattern such that, for a given beam, each sample received an identical range of fluences along its length. Analysis of the samples compared the performance of the untreated Al 6061 to that of the surface alloyed metal as a function of beam fluence.

Figure 30 shows the cross-section of a flashover diode-treated 80% Al - 20% Si surface with an original overlayer depth of 1 μm. The thickness of the melted layer averages 7 μm at the high fluence end and is negligible at the low fluence end. Most of the second phase particles are absent from the melted layer.

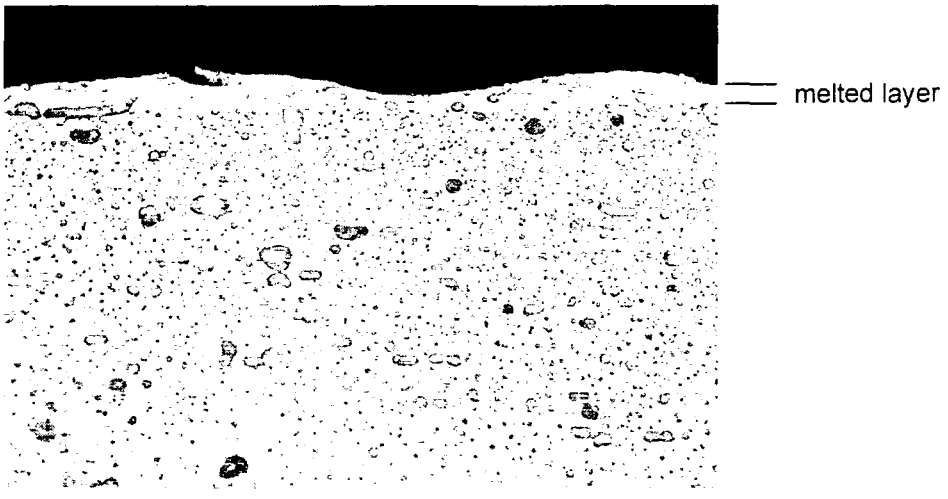

Figure 30. A micrograph of the cross section of Al 6061 with an 80% Al- 20% Si overlayer mixed into the surface by ion beam treatment with the flashover diode.

Wear tests were conducted using a linear reciprocating tribometer with a ball-on-flat geometry. For the test the counterface material was a 1/8-inch 440C steel ball bearing and a contact pressure of 0.8 GPa was used. Results for the 60% Al - 40% Si sample treated with the MAP nitrogen diode and the 80% Al - 20% Si sample treated with the flashover diode are shown in Figs. 31 and 32. The number of cycles to failure, which is defined as the number of cycles for the friction coefficient to reach 0.5, can be compared between the surface alloys and polished, untreated Al 6061 as a measure of the durability of the surface. The durability of the surface alloyed Al is a function of the fluence of the beam treatment, but in the best case, the durability of the Al-Si improves that of untreated aluminum by a factor of 100. Outside of these regions of "optimal" fluence, we see only slight improvements in durability over the untreated Al. Wear testing on the 60% Al - 40% Si overlayer sample (flashover diode) and the 80% Al - 20% Si overlayer sample (MAP Nitrogen diode) shows similar behavior with the optimal regions occurring in the middle fluence areas of the sample. The wear behavior of unmixed, RMR Al, shown in Fig. 33, is comparable to that of the mixed samples outside of the optimal regions.

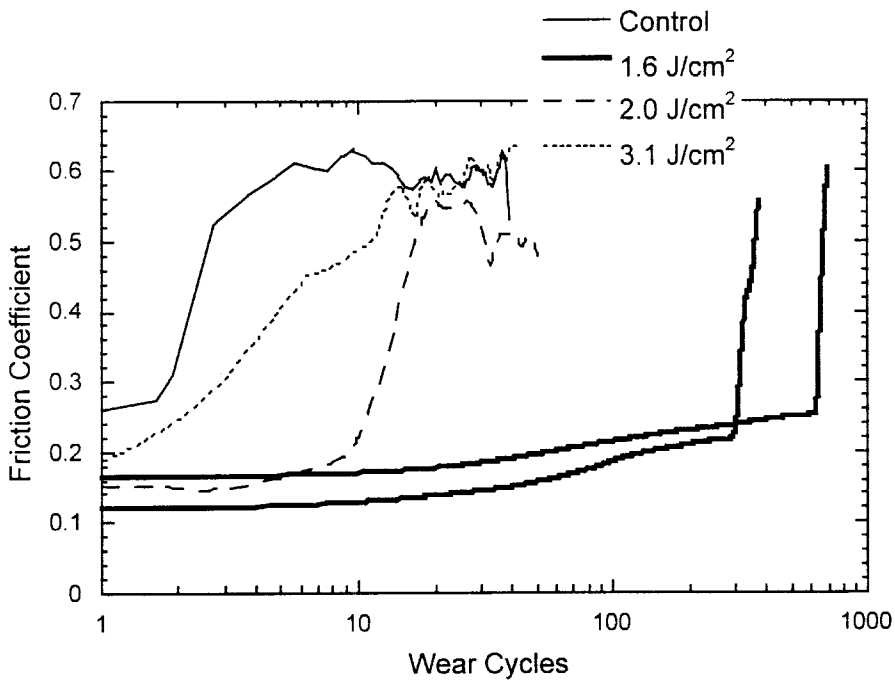

Figure 31. Wear test results for 60% Al Ð 40% Si surface alloyed by the MAP nitrogen diode.

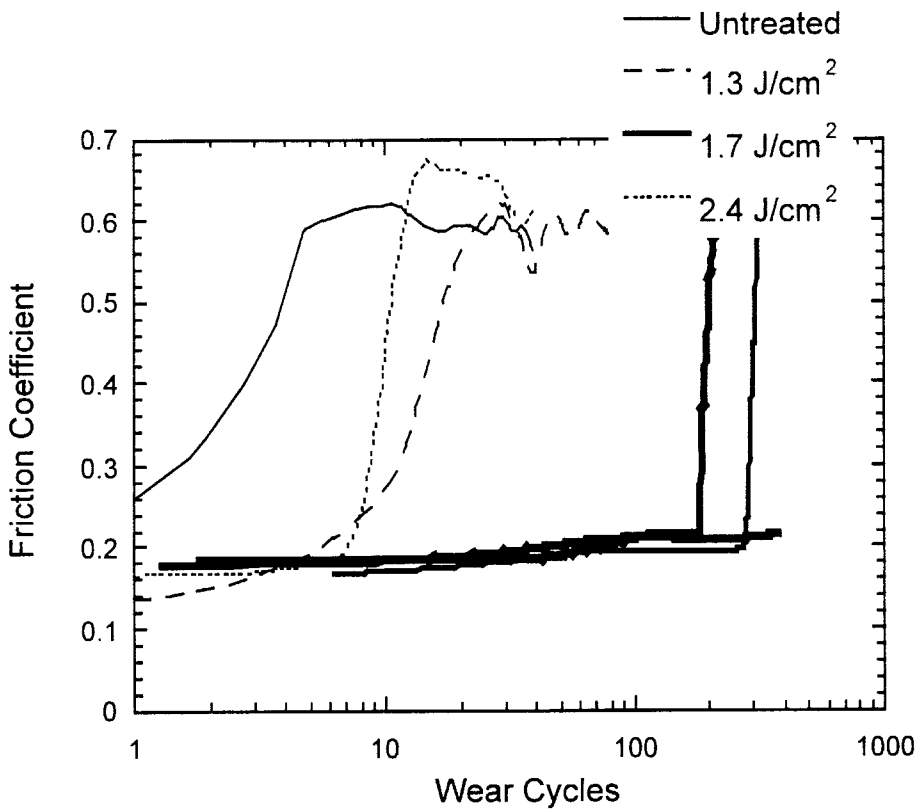

Figure 32. Wear test results for 80% Al - 20% Si surface alloyed by the flashover diode.

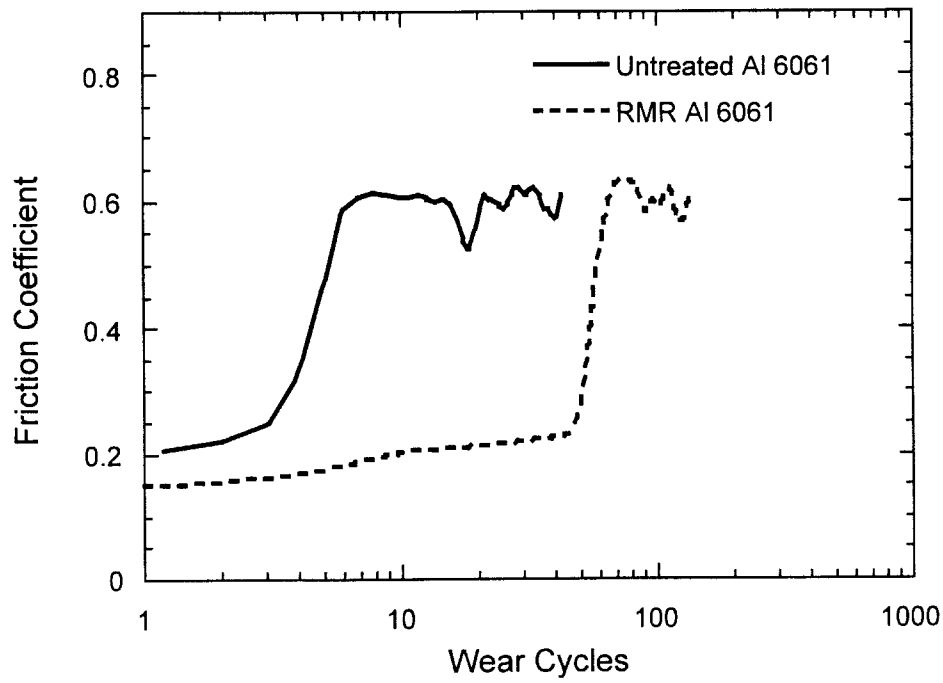

Figure 33. The durability of unmixed RMR Al 6061 is comparable to the durability of mixed, surface alloyed Al-Si in the non-optimal areas.

The hardness of the surface alloyed aluminum, measured by nanoindentation, is shown in Table 1. For the first three samples listed, the hardness was measured at locations corresponding to the regions of maximum durability. For the 80% Al - 20% Si overlayer sample (flashover diode) the hardness was measured at 4 equally-spaced intervals along the sample. In contrast to the strong dependence on durability with beam fluence, the hardness is nearly constant with beam fluence. The hardness values can be compared to the 0.6 GPa hardness measured for untreated Al 6061. The hardness of treated, unalloyed Al 6061 is 1.2 GPa. The softening seen at the lowest fluence may be due to annealing of the Al. But, since the thickness of the treated layer is less than 1 μm at the lowest fluence levels, the softness of the underlying material probably influences the hardness measurement. A thin, hard layer is most likely present over all areas of the treated sample.

Table 1. Surface hardness measured by nanoindentation for Al 6061 surface-alloyed with an 80% Al-20% Si or 60% Al-40% Si overlayer. Hardness values are relative.

Surface Hardness (GPa) of Surface Alloyed Al 6061 Hardness of untreated 6061 Al: 0.6 GPa					
Flashover Diode			MAP Diode - Nitrogen		
Fluence (J/cm^2)	80% Al-20% Si overlayer	60% Al-40% Si overlayer	Fluence (J/cm^2)	80% Al-20% Si overlayer	60% Al-40% Si overlayer
2.9			3.7		1.3
2.4	1.4		3.1		1.4
1.7		1.4	2.0		1.2
1.3			1.6	1.0	0.3

Optical surface profiling shows that the topography of the surfaces changes with the beam fluence. The samples, which were mirror polished prior to the treatment, display a surface pattern of hills and valleys after treatment. SEM images of the low, intermediate, and high fluence surfaces are shown in Fig. 34. As the beam fluence increases the amplitude of the hills and valleys increases. The spacing between the hills or wavelength of the surface generally decreases as the fluence increases. The decreased durability of the high fluence regions of the surface-alloyed material may be related to the topography of the surface. Imperfections in the surface can serve as initiation sites for wear. A buildup of wear particles leads to a rapid increase in the friction coefficient, as seen in Figs. 31-33.

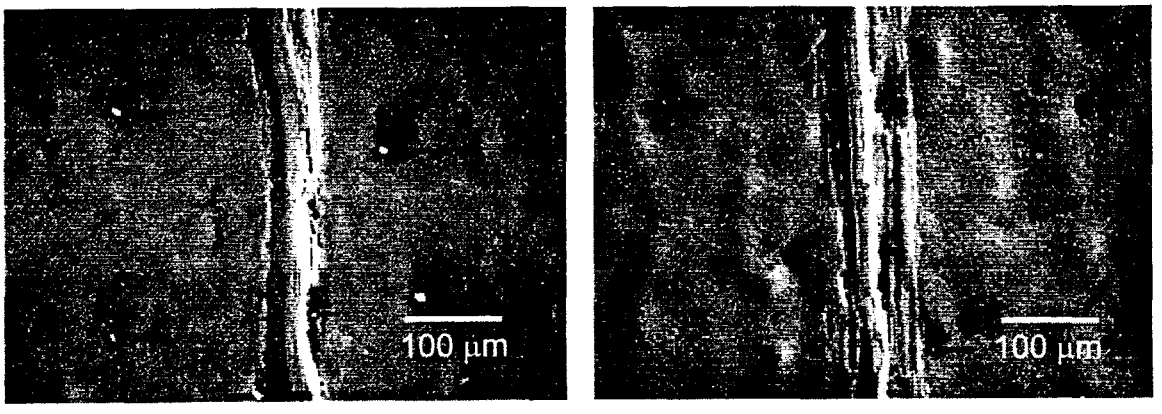

(a) (b)

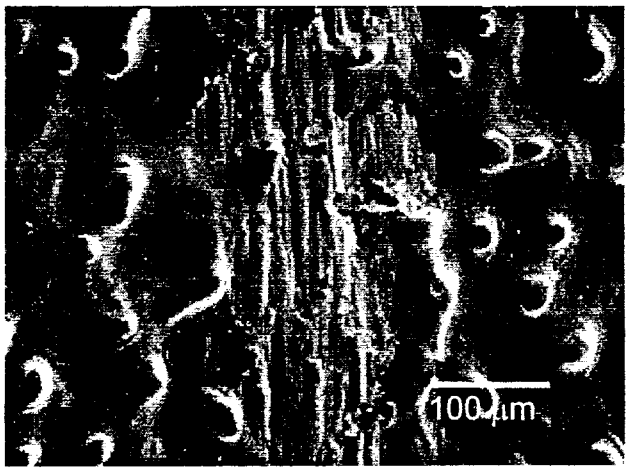

(c)

Figure 34. SEM images of wear tracks on surface-alloyed 80% Al - 20% Si with the MAP nitrogen diode at (a) low fluence, (b) intermediate fluence, and (c) high fluence levels.

Cross-sectional TEM (transmission electron microscopy) was used to examine the middle fluence portion of a 60% Al-40% Si overlayer sample treated with the flashover diode which corresponded to the region of maximum durability. Fig. 35 shows a TEM micrograph of the interface between the treated and untreated regions. Second phase particles present in the lower, untreated region are absent from the melted layer. The dark field TEM image of the melted layer in Fig. 36 shows small Si-rich particles approximately 10 nm in diameter. These particles are found in the top 1-1.5 µm of the 3 µm deep melted region. Microprobe analysis indicates that the Si concentration in the treated layer is ~ 3 wt.% at this fluence which exceeds the solid solubility limit for Si in Al. These metastable precipitates form as the sample is rapidly solidified. The presence of these small particles may account for the improvement in durability seen in this portion of the sample by improving the flow stress of the material.

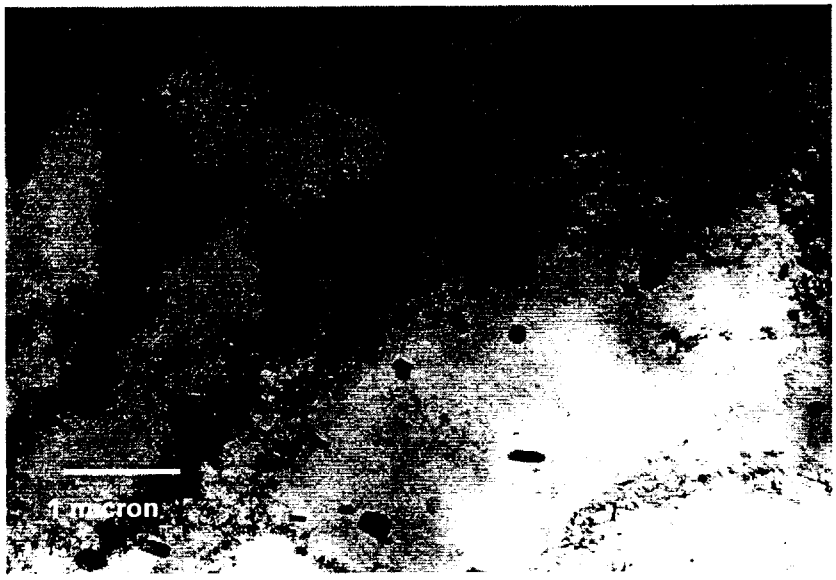

Figure 35. Transmission electron micrograph of the interface between the treated and untreated layers. The precipitates in the lower, untreated region are absent from the upper, treated region.

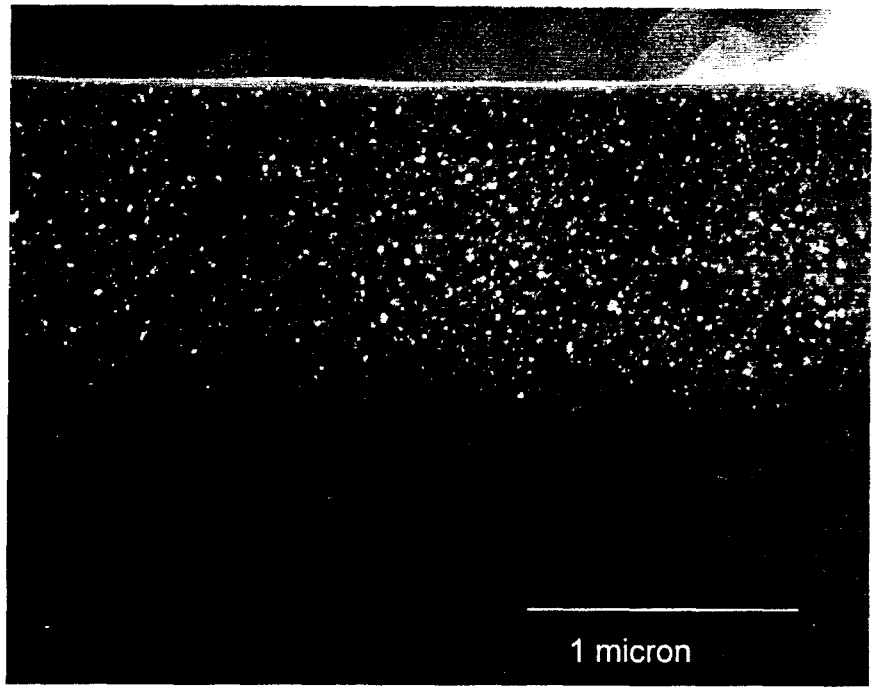

Figure 36. Dark field transmission electron micrograph showing the small silicon-rich precipitates found in the top 1-1.5 μm of the treated layer.

6.0 Surface Treatment Results for Titanium

From prior work, it was generally known that Ti alloys responded very favorably to pulsed ion beam treatment in the RMR mode. Efforts have focused on three Ti alloys 1.) Ti Grade 2, a commercially pure α-Ti, 2.) Ti Grade 12 (Ti-0.3Mo-0.8Ni), a near-α Ti, and 3.) Ti Grade 5 (Ti-6Al-4V), an α+β Ti alloy. In the RMR treatment mode, thick air-formed oxide films and mill scale are replaced by a thin thermal oxide which gives the alloy surface the appearance of being smoothed and polished. Surface roughness measurements show an actual physical smoothing effect. Ti alloys show reduced evidence of microcratering compared to Al and Fe surfaces, except when solid debris produced by the ion diode impinges on the sample surface.

Ti alloys are normally very corrosion resistant, but pitting can be induced in reducing environments (e.g. 1.0 M NaBr) when the alloys are polarized 1 to 2 V positive to their rest potential. Corrosion resistance is degraded by additions of certain alloying elements, notably Al in Grade 5 Ti. RMR treatment of Ti Grade 5 has been shown to eliminate pitting susceptibility to potentials up to 2.0 V.

Corrosion resistance of Ti alloys depends on the integrity of a tenacious oxide film. Localized corrosion can occur if this film is mechanically damaged. It is known that noble metal additions promote oxidizing conditions at Ti alloy surfaces that stimulate healing of damaged films, a phenomenon otherwise known as repassivation. Ti Grade 7 has 0.15 weight % Pd intentionally added to induce just this effect. We have mixed Pd and Pt into the surfaces of Ti alloys to promote repassivation. Results obtained from electrochemical testing of Pt-Ti surface alloys indicate that film thickening and metastable pitting occur consistent with enhanced passivation.

Ti alloys are poor tribological materials due to relatively low tensile and shear strengths. However properties such as a high strength/density ratio and biomedical compatibility makes Ti alloys useful in turbine components, aviation applications, and in prosthetic devices. Surface treatments to reduce friction and wear expand the range of Ti alloy applications to those where tribological effects are important.

6.1 Corrosion Resistance of RMR Treated Titanium Alloys.

Corrosion testing has been conducted on Ti Grade 2 (commercially pure α-Ti) and Ti Grade 5 (Ti-6Al-4V, α+β Ti) to determine if ion beam treatment can successfully improve corrosion resistance. Titanium is normally very corrosion resistant due to a tenacious TiO_2 oxide film. However, Ti and Ti alloys are susceptible to localized corrosion in reducing environments. Therefore corrosion testing was conducted in a 1.0 M NaBr solution (which is reducing to TiO_2) to stimulate pitting at relatively low applied potentials.

Figure 37 shows anodic polarization curves for treated and untreated Ti Grade 2 in 1.0 M NaBr solution. A comparison of the curves shows that the passive current density for the treated sample is reduced by nearly two orders of magnitude compared to its untreated counterpart. Additionally, the treated sample exhibits no stable pitting up to 2.0 V_{sce}, which was the highest potential reached during the scan. By comparison, pitting is observed in the untreated control sample at approximately +1.7 V_{sce}. This result shows that ion beam treatment can improve the localized corrosion resistance of commercially pure Ti.

Improvements in corrosion resistance have also been demonstrated with Ti Grade 5. Ti Grade 5 differs from Grade 2 in that it contains substantially more alloying elements. These alloying elements are added to improve mechanical properties, but have been shown to have a negative effect on corrosion resistance (particularly Al additions). Figure 38 shows anodic polarization curves for treated and untreated Ti Grade 5. The passive current density was reduced by an order of magnitude and a substantial improvement in the pitting potential was observed. The untreated control sample pitted at approximately +0.900 V_{sce}, while no pitting was observed up to the highest pitting potential tested which was +2.0 V_{sce}.

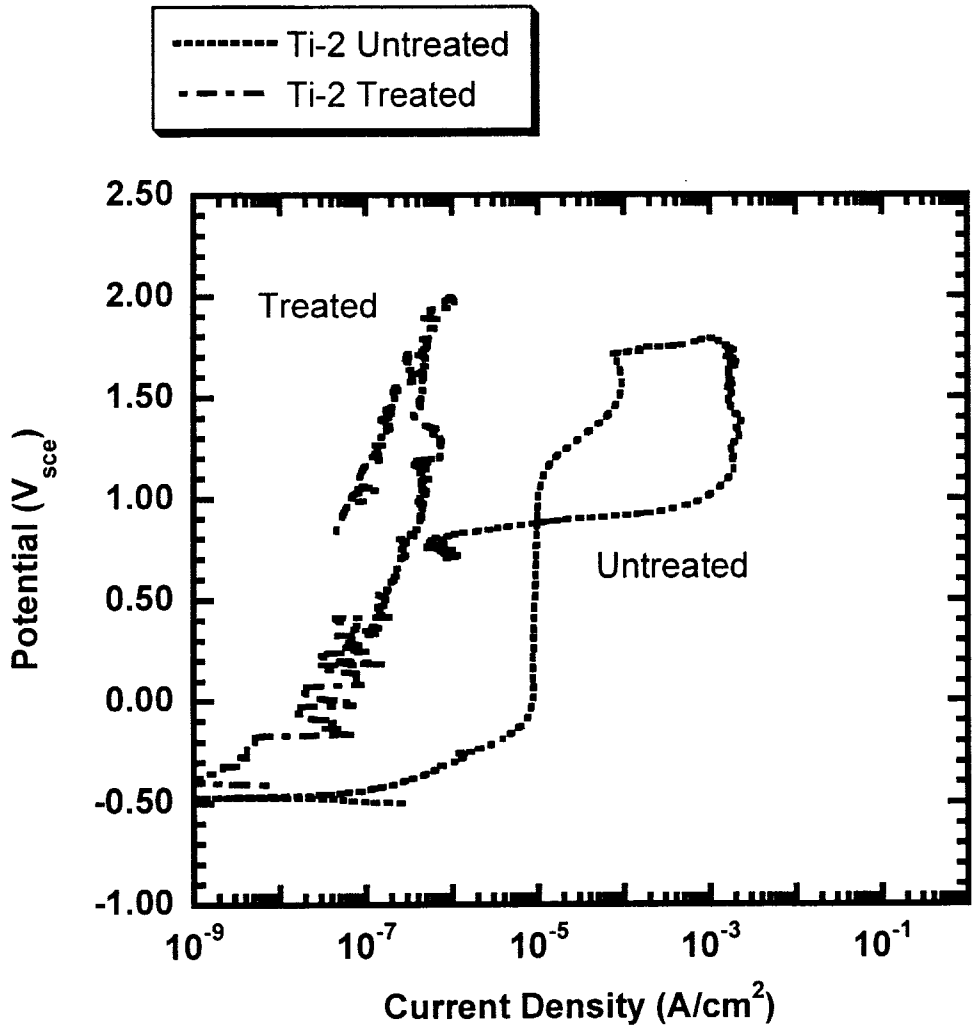

Figure 37. Anodic polarization curves for treated and untreated Ti Grade 2 in 1.0 M NaBr solution showing improved corrosion resistance after ion beam treatment.

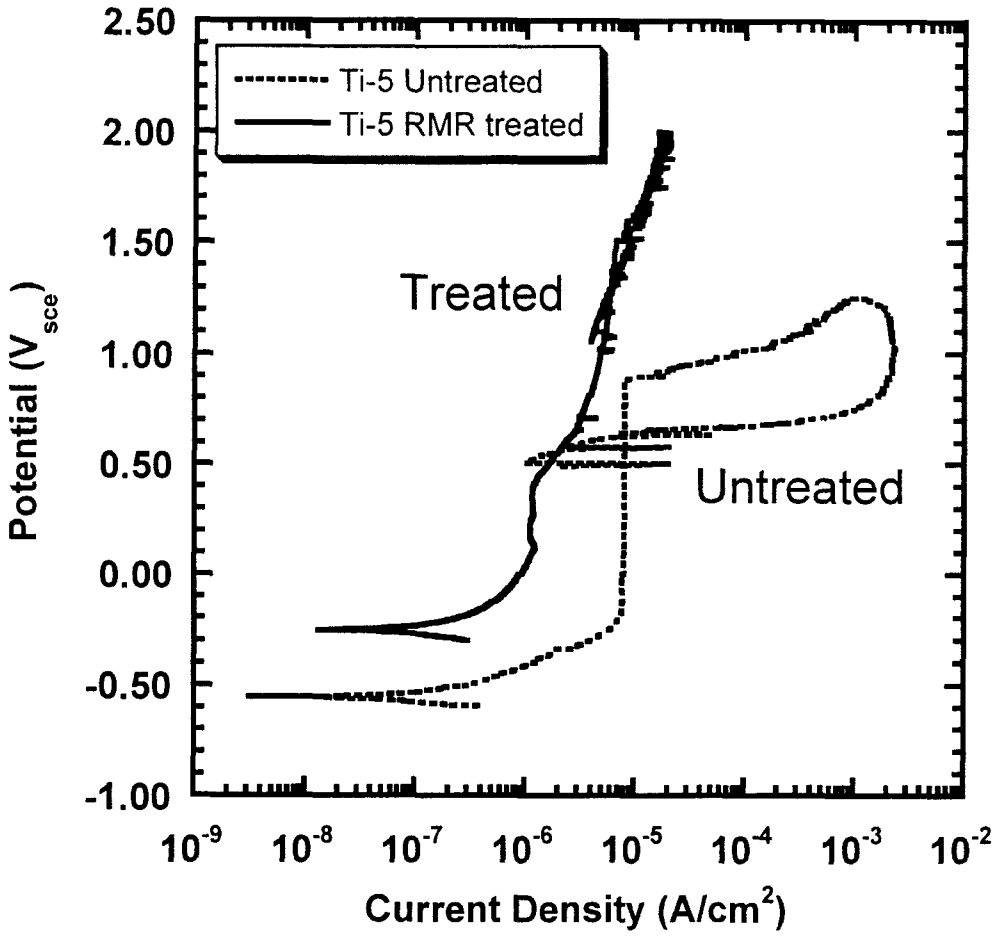

Figure 38. Anodic polarization curves for treated and untreated Ti Grade 5 in 1.0 M NaBr solution showing improved corrosion resistance after ion beam treatment.

6.2 Corrosion Resistance of Surface Alloyed Titanium.

Noble metal additions to Ti are known to promote stability of the passivating TiO_2 film by helping to maintain oxidizing conditions at the alloy surface. Ti Grade 7 has 0.15 % Pd intentionally added for this reason. Other noble metals, including Pt, act in a similar fashion. Pt on Ti samples were prepared to determine if a positive effect on corrosion resistance could be imparted by forming a Ti-Pt surface layer. Samples were prepared by sputter depositing Pt on to Ti Grade 2 in thickness ranging from 1600 to 20000 Å. Samples were then subjected to multiple pulse beam treatment. The thick Pt layer samples were treated using large τ, large n treatments. These samples were then tested for corrosion resistance by conducting anodic polarization in 1.0M NaBr solution. The results from these test are shown in Table 2. Pitting was detected on the blank, 1600 Å, 11400 Å, and 20000 Å Pt samples. It is suspected that the thicker Pt layers were not completely mixed into the substrate thereby inducing some localized corrosion susceptibility. Clearly these data show that for these treatment conditions there is an optimal Pt thickness range for which corrosion resistance is maximized. Characterization experiments are underway to identify structure and composition of the treated layers in these samples.

Table 2. Summary of anodic polarization results for mixed Pt-Ti tested in 1.0 M NaBr solution.

Pt thickness (Å)	E_{oc} (V_{sce})	E_{pit} (V_{sce})	E_{rp} (V_{sce})	i_{pass} ($\mu A/cm^2$)
0	-0.11	1.86	0.68	0.77
1600	-0.03	< 2.0	0.81	50.5
2400	-0.09	> 2.0	> 2.0	0.76
4100	-0.95	> 2.0	> 2.0	0.95
11400	0.04	< 2.0	1.6	1.60
20000	-0.27	< 2.0	1.7	189

To assess the effect of IBEST treatment on Ti alloys, potentiodynamic polarization experiments were run in aggressive reducing environments (1.0N NaBr). From the polarization curves, pitting information can be extracted. Figure 39 is a plot of pitting potential for a number of Ti-5 and Ti-2 alloys.

In general, adding noble metals to the Ti matrix results in an increase in pitting potential, or increased resistance to pitting. Although it is impossible to generalize the effects of alloying additions or surface treatment, the following points can be made:

- Mixing Nb into Ti-5 improves the pitting resistance.
- Adding Pt to Ti-5 improves pitting resistance. However, mixing the surface reduces the improvement substantially. This suggests that the surface may not be mixed homogeneously.
- Treatment of bare Ti-5 provides some improvement in pitting resistance. It appears that the MAP nitrogen beam is more effective in reducing pitting than is MAP Ar.
- Pt is more effective than Nb in improving the pitting resistance of Ti-2.

Figure 40 shows the substantial effect on the electrochemical behavior of Grade-2 Ti, when Pt is surface-alloyed into Ti,. The untreated sample undergoes pitting at about 1.7 V (SCE). It exhibits a wide stable passive region, and repassivates at fairly high potentials. The RMR treated sample exhibits a lower passive current density and is immune to pitting up to 2 V. The open circuit potential is almost identical to the untreated sample. It is probable that the improved passivation behavior and pitting resistance is the result of a modified passive oxide that forms during the treatment process. The third curve in Figure 40 is for a mixed Pt-Ti sample. The beam treatment causes mixing of the Pt into the Ti and results in between 3% and 7% Pt in the alloy. Consistent with the presence of Pt in the alloy, the open circuit potential is shifted about 0.5 V in the noble direction to around 0 V. There is no distinct passive region, but from about 0.2 to 0.8 V(SCE), there is evidence of metastable pitting. The current increases rapidly above 0.8 V, and at 1.5 V is almost 2 orders of magnitude higher than for the untreated sample. However, the increased current density is not due to pitting, as both the reverse polarization behavior and visual examination of the surface following the experiment failed to indicate any pitting. The electrochemical behavior at potentials above 0.8 V is consistent with oxygen evolution, and indicate that the water oxidation reaction is catalyzed due to the presence of the Pt.

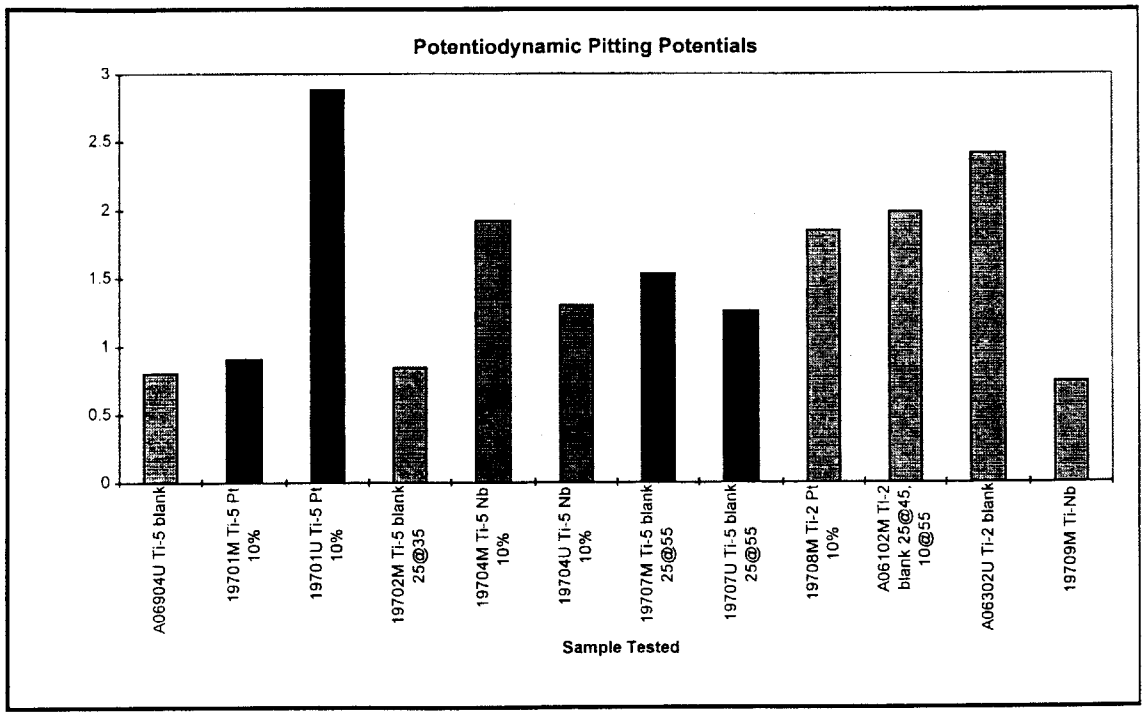

Figure 39. Pitting potentials determined from potentiodynamic polarization curves. Substrates were Grade-2 and Grade-5 Ti, some with Pt or Nb layers deposited prior to mixing.

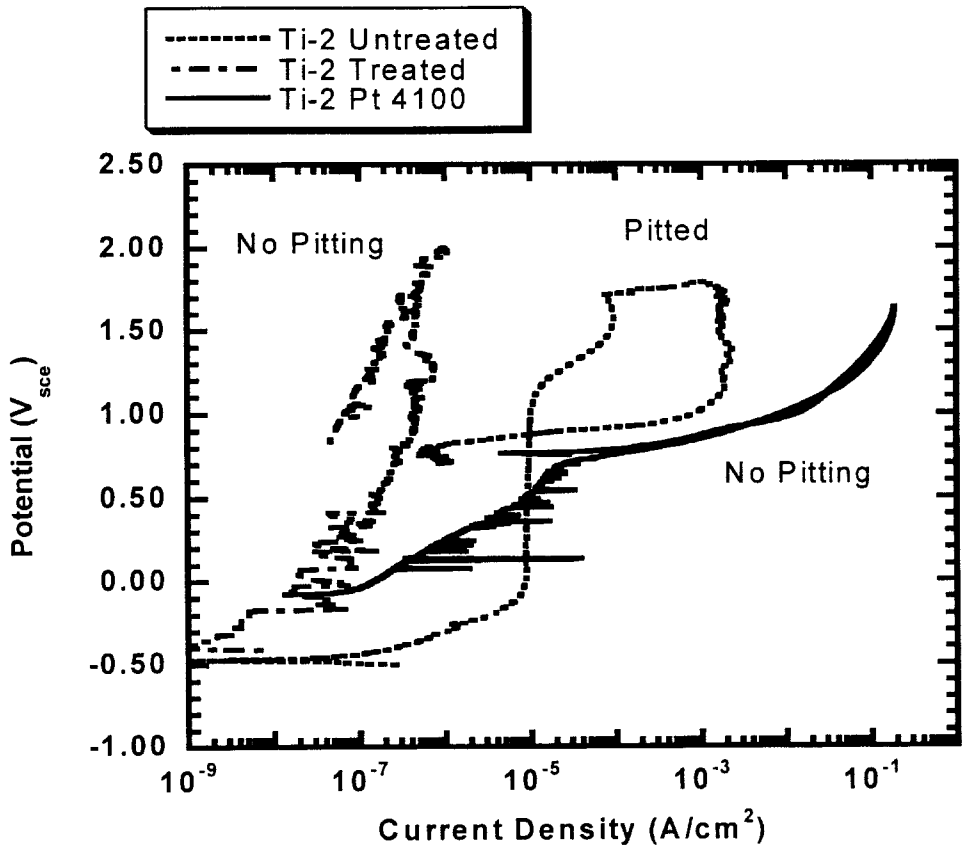

Figure 40. Potentiodynamic polarization behavior for Grade-2 Ti in 1.0N NaBr. The addition of Pt to the alloy substantially alters the electrochemical response.

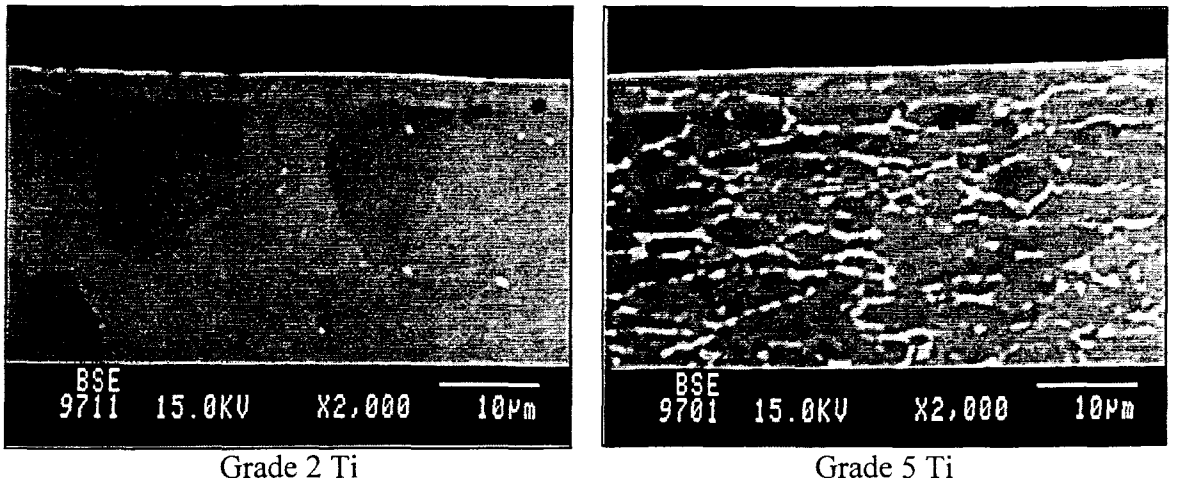

Grade 2 Ti Grade 5 Ti

Figure 41. Electron microprobe images of Ti-2 and Ti-5 cross sections. Note the absence of structure in the mixed layer.

IBEST treatment of Ti-2 and Ti-5 has been shown to alter the microstructure. In particular, there appears to be some convecting and homogenization of the surface that takes place. Figure 41 presents cross section micrographs of Ti-2 and Ti-5 after treatment. Note the absence of structure, particularly in the Ti-2 sample. The treated layer is clearly visible, and the distinct grains appear to stop at that layer. While less pronounced in the Ti-5 sample, there is still evidence of homogenization of the treated layer, with less pronounced grain boundaries and beta phase Ti present.

6.3 Surface Alloying and Hardening of Titanium

The surface alloying of titanium with Nb or Pt has been investigated. The titanium was treated with the MAP source using either N or Ar ions. Hardness of the treated samples were improved by a factor of 3 in some cases (Table 3). The durability of all the treated samples exceeded the durability of untreated titanium. Treatment of pure Pt layers on Ti Grade 5 resulted in incomplete mixing leaving a layer of Pt on the surface. These surfaces showed improvements in durability. However, the increase in performance may have been due to the softer Pt on the surface.

Wear testing of a Ti Grade 5 sample surface alloyed with a 90% Ti - 10% Pt layer using the MAP nitrogen diode shows increased durability as compared to both untreated Ti Grade 5 and treated, unalloyed Ti Grade 5 as shown in Fig. 42. The wear test was conducted with a linear reciprocating tribometer using a 1/8-inch 440C ball bearing counterface and a contact pressure of 0.8 GPa. These results also show that the initial friction coefficient of the treated samples is 0.3 whereas the initial friction coefficient of the untreated sample is below 0.1, perhaps due to the increased roughness of the treated sample as compared to the mirror finish of the untreated control. The surface oxide layer of the untreated Ti Grade 5 is breached in less than 10 cycles as indicated by the rapid rise in friction coefficient. The treated surface maintains a friction coefficient below 0.35 for at least 200 cycles due to its increased hardness. The wide variation in the results for the surface alloy is probably due to the surface roughness of the treated sample.

Table 3 Hardness of Surface Alloyed Titanium

Substrate	Alloying Element	Diode	#shots@ distance (cm)	Hardness (GPa)
Ti-5	10% Pt	MAP Ar	25@35	2.9
Ti-5	none	MAP Ar	25@35	0.8
Ti-2	10% Pt	MAP Ar	25@35	1.9
Ti-5	10% Nb	MAP Ar	25@35, 50@55	3.8
Ti-5	none	MAP N	25@55	4.4
Ti-2	10% Pt	MAP N	25@55	4.4
Ti-5	10% Nb	MAP N	117@55, 25@55 50@55	4.7
Ti-5	10% Nb	MAP N	50@55	1.9
Ti-5	10% Nb	MAP N	117@55	1.4
Ti-5, untreated				1.5

SEM photos of the wear tracks on the untreated Ti Grade 5 sample, untreated Ti Grade 5 sample with the 90% Ti- 10% Pt overlayer, and the treated, surface alloyed 90% Ti- 10% Pt overlayer sample are shown in Fig. 43 (a), (b), and (c), respectively. The wear track in Fig. 43(c) corresponds to a wear test run for 2000 cycles and shows negligible wear compared to the untreated samples. Undulations in the treated surface prohibit quantitative measurements of the wear rate. The polished cross section of this surface alloyed Ti-Pt sample is shown in Fig. 44. The hardened, treated layer has resisted mechanical polishing and in several areas protrudes from the cross-section by 2 μm. Other areas in the treated layer are recessed by ~ 2 μm from the removal of grains in a pattern resembling intergranular fracture.

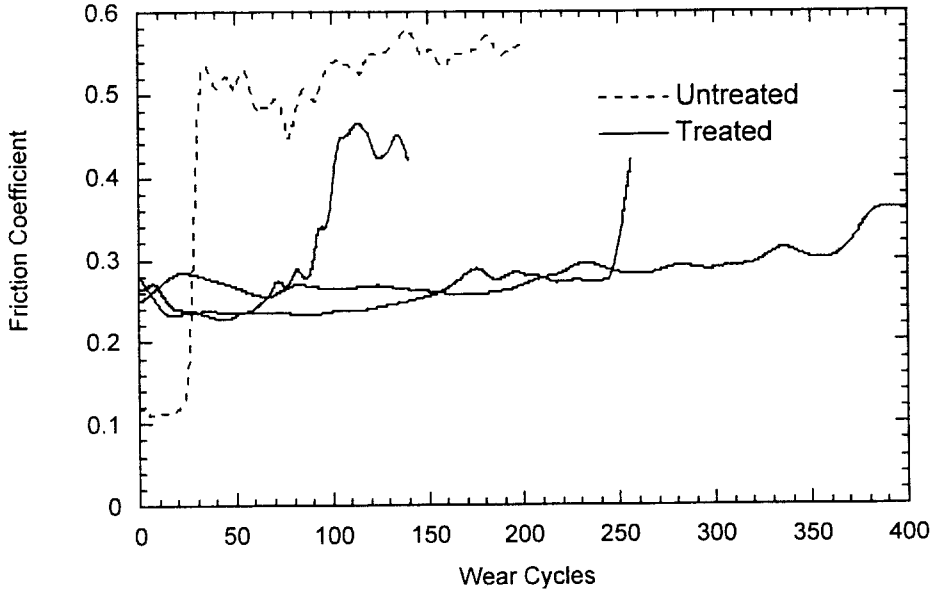

(a)

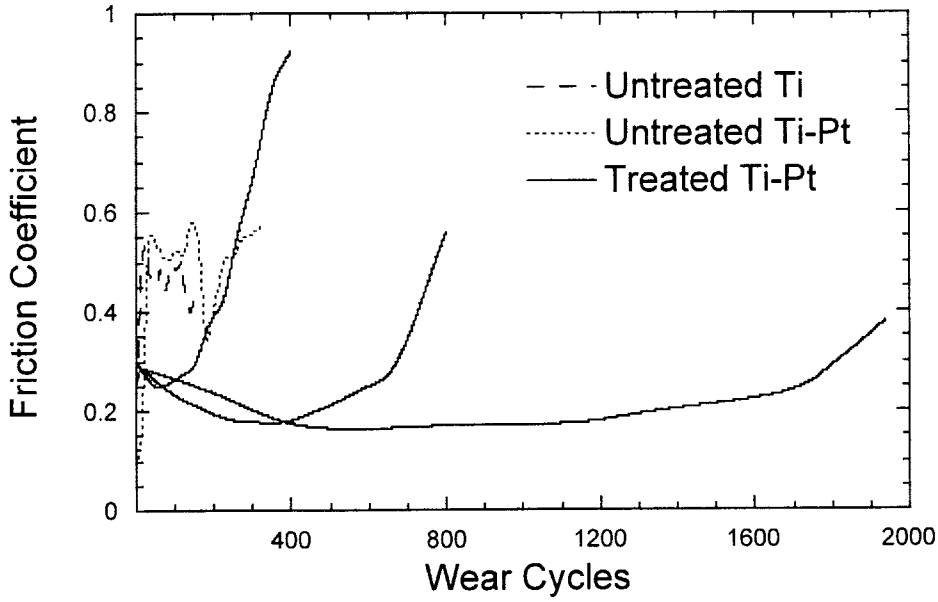

(b)

Figure 42. (a) Wear test results for unalloyed Ti Grade 5. (b) Surface alloying of Ti Grade 5 with a 90% Ti - 10% Pt layer improves the tribological performance over untreated Ti Grade 5.

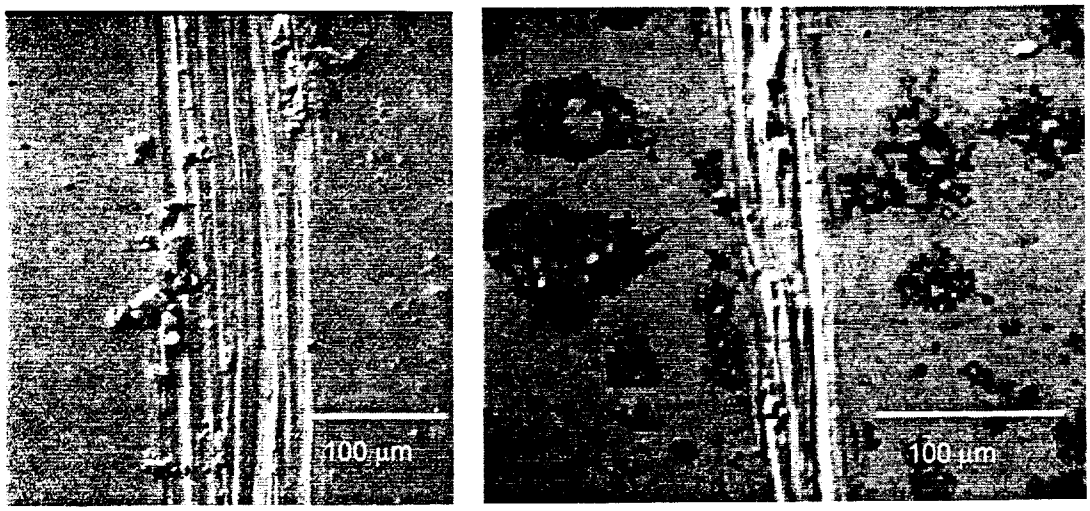

(a) (b)

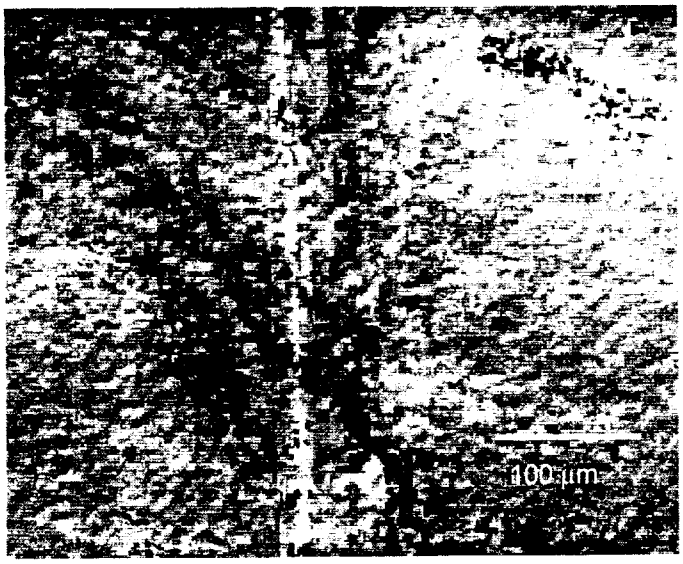

(c)

Figure 43. Wear scars for (a) untreated Ti Grade 5 sample, (b) untreated Ti Grade 5 with Ti-Pt overlayer, (c) Ti Grade 5 with Ti-Pt overlayer and IBEST treatment showing negligible wear.

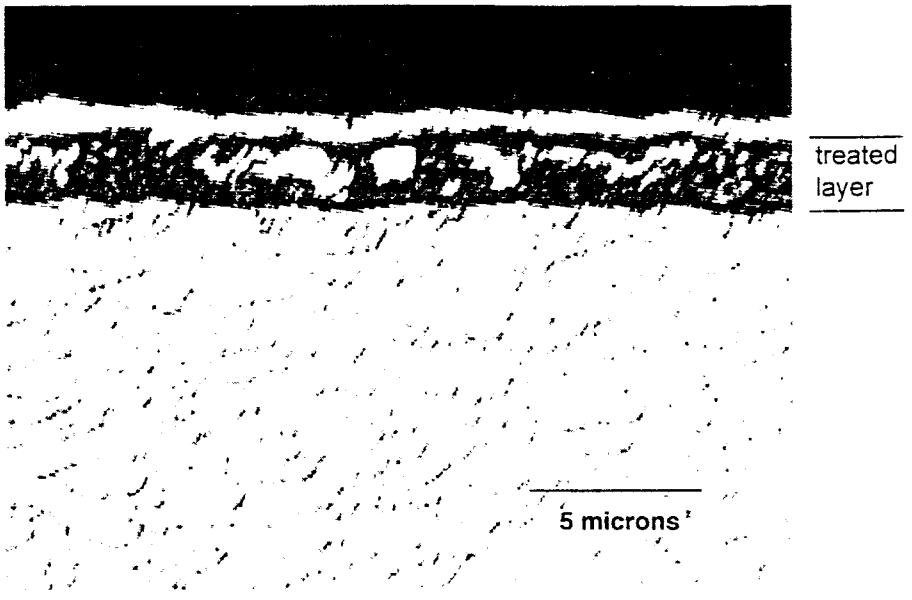

Figure 44. The polished cross-section of the surface alloyed Ti-Pt sample shown in Fig. 37(c). The light-colored layer at the top is plated Ni to protect the edge during cutting and polishing. The bright areas within the treated layer are grains protruding from the polished surface.

6.4 Surface Smoothing of Titanium

Titanium responds in a very favorable way to pulsed ion beam treatment. Upon treatment the surface is smoothed and thick oxide films are removed. Table 4 below illustrates the surface smoothing that is obtained as the total number of pulses increases. Surface roughness measurements were obtained using an optical interferometry technique. An average E_d of 4 to 5 J/cm^2 was estimated at the point where the measurements were made.

During the code validation study detailed in Section 3, we made reflectometry measurements using Ti targets instead of Si, and monitored the behavior of the reflection coefficient over a series of shots. The injected gas was Argon, which yielded a mixed beam consisting of carbon and argon in various charge states. Starting from a mirror finish, the first pulse clearly roughened the surface, as indicated by a reduction in reflected laser light. On subsequent pulses, however, the reflected signal increased steadily, reaching the original reflectance level after about 5 shots. This is consistent with our experience with heavier ion beams, that post-treatment surface topography is smoother than when protons are used. Furthermore, Ti surface smoothness is retained by heavier ion treatment, in contrast to Al, which continually roughens with the number of pulses.

Table 4. Surface roughness data for Ti Grades 2,5, and 12.

	Average Surface Roughness (nm)		
Treatment	**Ti Grade 12**	**Ti Grade 2**	**Ti Grade 5**
untreated	675-852	263-273	413 - 456
1 pulse	786	250	413
5 pulses	403	194	337
10 pulses	283	231	209

7.0 Conclusions

We have used the emerging technology of repetitive pulsed intense ion beams (IBEST) to rapidly heat and cool the surface of three types of metal alloys - aluminum, iron, and titanium. We have also investigated surface alloying, where the beam is used to mix a predeposited thin-film coating over the three substrates. The goal in either case has been 1) to produce improvements in surface corrosion resistance and/or surface hardness and wear durability and understand their microstructural basis; and 2) to produce a prescription for treatment (e.g. number of pulses, fluence level, treatment ion(s)) in each case that would serve as a basis for a commercially viable process.

Improvements to surface corrosion resistance, hardness, and wear durability have been demonstrated for all three metal alloys systems investigated. Melt depths of up to 10 microns, and melt durations up to 5 microseconds have been observed, and results benchmarked with a 1-D code. In the process, we have developed a viable technique for the surface processing of silicon that has potential use in both the semiconductor and solar industries. We have observed beam-induced hardening on a length scale of tens of microns, or well beyond the melt zone, in stainless steel, corroborating what has been routinely reported by Russian researchers.

We summarize specific results for the three alloys groups:

1) **Iron:** Both corrosion resistance and surface wear durability have been improved by IBEST treatment. We believe the mechanism for improvement is dispersal of second-phase particles. Some additional improvements in corrosion resistance have been produced by mixing of Cr into the surface. We have seen deep-lying improvements in hardness as far as 100 microns below the surface, although not on a consistent basis.
2) **Aluminum:** This alloy is subject to more extensive microcratering and roughening than the other alloy groups, caused we believe by the relatively low melting point of Al, and deep ion penetration distances in Al. Also, Al has not been as amenable to surface improvements by simple IBEST processing (i.e. without surface alloying) as have the other alloy groups. Significant improvements in corrosion resistance have been observed by mixing with transition metals, most notably with hafnium. Improvements in wear durability have been produced by mixing silicon into the surface. In the case of Si, hardness improvements are consistent across a range of treatment intensities, but improvements in durability are limited to a narrow fluence range.

3) **Titanium:** Under beam treatment, Ti processes to a smoother surface than the other two alloy groups. Simple surface modification of Ti alloys without surface alloying have led to improvements in corrosion resistance. Some additional improvement has been observed by the mixing of Pt into the surface. Although IBEST treatment of Ti alone has produced improvements in surface hardness and wear durability, more significant gains have been seen by mixing in of Pt.

8.0 References

1. W. Klement, Jr., R. H. Willens, and P. Duwez, Nature, 187, 869 (1960)
2. T. Masumoto and R. Maddin, Trans. Met. Soc AIME, 245, 2475 (1969)
3. T. R. Anantharaman and C. Suryanarayana, in Rapidly Solidified Metals: A Technological Overview (Trans Tech Publications, Switzerland, 1987.
4. Rapidly Solidified Alloys, ed. by Howard H. Liebermann (Marcel Dekker, Inc., New York, 1993)
5. D. Raybould, Metal Powder Rep., 39, 282 (1984)
6. Anon, Precision Metal, 40(3), 19 (1982)
7. K. Asami, A. Kawashima, and K. Hashimoto, Mater. Sci. Eng., 99, 475 (1988).
8. R. Ray and T. A. Mozhi, Metal Powder Rep. 44, 129 (1989).
9. G. J. Yurek, D. Eisen, and A. Garratt-Reed, Metall. Trans. A, 13A, 473 (1982).
10. T. Tsuru, S. X. Zhang, and R. M. Latanision, in Rapidly Quenched Metals IV, edited by T. Masumoto and K. Suzuki (The Japan Inst. Metals, Sendai, 1982) p. 1437.
11. T. F. Broderick, A. G. Jackson, H. Jones, and F. H. Froes, Metalll. Trans. A, 1 A, 1951 (1985).
12. J. C. Bittence, Mater. Eng., 95(4), 57 (1982).
13. N. Amano. Y. Odani, Y. Takeda, and K. Akechi, Metal Powder Rep., 44, 186 (1989).
14. Reference 4, p746
15. J. B. Lumsiden, D. S. Gnanamuthu, and R. J. Moores; in "Corrosion of Metals processed by directed energy beams", (ed. C. R. Clayton and C. M. Preese), 129-134; 1982, Warrendale, Pa. Metallurgical Society of AIME.
16. C. J. Lin and F. Spaepen, Appl. Phys. Lett., 1982, 41, 721-723.
17. E. M. Breinan, B. H. Kear, L. E. Greenwald, and C. M. Banas, "Laser Glazing, a New Process for Produ ction and Control of Rapidly Chilled Metallurgical Microstructures," Lasers in Modern Industry, (Dearborn, Michigan 1979), 147-166.
18. H.-W. Bergmann, B. L. Mordike, "Laser and Electron-Beam Melted Amorphous Layers,"J. Mat. Sci., (1981), 863-869.
19. Joe E. Jenkins, "Surface Modification by Electron Beam Glazing," Thin Solid Films, 84 (1981), 341-346.
20. G. E. Remnev, and V. A. Shulov, "Practical Applications of High-Power Ion Beams," 9th International Conference on High-Power Particle Beams, Washington, D.C., 5/25-29, 1992.
21. S. A. Chistjakov, A. M. Gagarin, R. G. Koishibaev, Yu Yu Rjuchkov, V. A. Kuzminikh, V. M. Milutin, V. A. Pirogov, V. A. Perov, A. D. Pogrebnjak, S. V. Plotnik, G. E. Remnev, Yu G. Rusin, and V. P. Janovskii, "Ion Mixing of Near Surface Layers in Au-Cu, Cu-Mo Systems Irradiated by HPIB," Physics Letters, Vol. 131, No. 1, 8/1, 1988, 73-77.
22. V. L. Kutuzov, M. Yu. Ovsyannikov, I. G. Romanov, A. D. Pogrebnk, and G. E. Remnev, "Mechanical and Frictional Properties of Tool Steels Exposed to HPIB Irradiation," Mechanical and Frictional Properties of Tool Steels, 11/8, 1988, 361-364.
23. Y. Shimotori, et al., JAP 63, 968 (1988).
24. R. Fastow, "Pulsed Ion Beam Surface Modification of Materials", Ph.D. thesis, Cornell University, 1985.
25. R. Fastow, Y. Maron, and J. Mayer, "Pulsed ion beam melting of silicon", Phys. Rev. B, 31,893 (1985).

26. R. W. Stinnett, R. G. Buchheit, F. A. Greulich, C. R. Hills, A. C. Kilgo, D. C. McIntyre, J. B. Greenly, M. O. Thompson, and D. J. Rej, "Thermal Surface Treatment Using Pulsed, Intense Ion Beams", Mat. Res. Soc. Symp. Proc. 316, 521 (1994).
27. H. C. Harjes, K. J. Penn, K. W. Reed, C. R. McClenahan, G. E. Laderach, R. W. Wavrik, J. L. Adcock, M. E. Butler, G. A. Mann, G. E. Pena, G. J. Weber, D. VanDeValde, L. E. Martinez, D. Muirhead, P. D. Kiekel, D. L. Johnson, E. L. Neau, "Initial results from the RHEPP module", Proc. 9th Int. Conf. on High Power Particle Beams, Washington D.C., May 25-29, 1992, 333-340.
28. J. B. Greenly, M. Ueda, G. D. Rondeau and D. A. Hammer, "Magnetically Insulated Ion Diode with a Gas-Breakdown Plasma Anode," J. Appl. Phys 63, 1872 (1988).
29. J. B. Greenly, L. Brissette, A. Dunning, S. C. Glidden, D. A. Hammer and W. A. Noonan, "Plasma Anode Ion Diode Research at Cornell: Repetitive Pulse and 0.1 TW Single-Pulse Experiments," Proceedings of the 8th Intl. Conf. on High Power Particle Beams, B. N. Breizman and B. A. Knyazev, Eds., Novosibirsk, 1990 (World Scientific), p. 199.
30. Trim90, J. F. Ziegler, IBM, T. J. Watson Research Center, Yorktown Heights, NY
31. M. O. Thompson and T. J. Renk, "Numerical Modeling and Experimental Verification During Pulsed Ion Beam Treatment", to be published in Proceedings of the Materials Research Society.
32. V. P. Rotshtein, D. I. Proskurovsky, and G. E. Ozur, "Surface Treatment of Metallic Materials with Low Energy, High-Current Electron Beams", Fifth International Conf. On Electron Beam Technologies", Varna, Bulgaria, June2-5, 1997, G. M. Mladenov, Editor.

DISTRIBUTION:

Unclassified Unlimited Release

External Distribution:

10 Regan Stinnett
Mark Crawford
Tom Lockner
Dale McIntyre
QM Technologies
3701 Hawkins Street, NE
Albuquerque, NM 87109

10 Prof. Rudolph G. Buchheit
The Ohio State University
Fontana Corrosion Center
Dept. of Materials Science and Engineering
477 Watts Hall
2041 College Road
Columbus, OH 43210-1187

1 Dr. Kenneth S. Grabowski
Code 6670, Building 74
Naval Research Laboratory
4555 Overlook Ave., SW
Washington, DC 20375

10 Professor Michael O. Thompson
Department of Materials Science
Bard Hall
Cornell University
Ithaca, NY 14853

10 Donna Senft
Permacharge Corporation
5930 Midway Park, NE
Albuquerque, NM 87109

5 Dr. Walter M. Polansky
DOE/ER-32

Internal Distribution:

1	MS9018	Central Technical Files, 8940-2
2	MS0899	Technical Library, 4916
2	MS 0619	Review & Approval Desk, 12690 for DOE/OSTI
1	MS0151	Gerry Yonas, 9000
10	MS0340	N. R. Sorensen, 1832
5	MS0340	W. R. Cieslak, 1832

1	MS0513	R. J. Eagan, 1000
1	MS1056	B. L. Doyle, 1111
1	MS1056	C. J. Barbour, 1111
1	MS1056	J. A. Knapp, 1111
1	MS1056	D. M. Follstaedt, 1112
1	MS1056	S. M. Myers, Jr., 1112
1	MS1152	M. L. Kiefer, 9542
1	MS1152	L. X. Schneider, 9543
1	MS1178	J. A. Hands, 9516
1	MS1178	J. J. Ramirez, 9580
1	MS1178	P. S. Raglin
1	MS1181	J. R. Asay, 9511
20	MS1182	T. J. Renk, 9514
20	MS1182	B. N. Turman, 9514
1	MS1182	D. D. Bloomquist, 9530
1	MS1184	F. W. Long, 9537
1	MS1186	T. A. Mehlhorn, 9574
1	MS1187	K. M. Matzen, 9570
1	MS1187	J. L. Porter, 9573
1	MS1188	R. A. Hamil, 9512
1	MS1190	D. L. Cook, 9500
1	MS1191	J. P. Quintenz, 9500
1	MS1193	J. E. Maenchen, 9515
1	MS1194	D. H. McDaniel, 9540
1	MS1194	R. B. Spielman, 9544
1	MS1196	R. J. Leeper, 9577
1	MS1421	G. A. Samara, 1152
1	MS1427	S. T. Picraux, 1100
1	MS1434	G. E. Pike, 1900
1	MS9999	V. S. Roberts, 9591